Turbulence as a Mechanism for Orographic Precipitation Enhancement

ROBERT A. HOUZE JR. AND SOCORRO MEDINA

Department of Atmospheric Sciences, University of Washington, Seattle, Washington

(Manuscript received 30 January 2004, in final form 25 August 2004)

ABSTRACT

This study examines the dynamical and microphysical mechanisms that enhance precipitation during the passage of winter midlatitude systems over mountain ranges. The study uses data obtained over the Oregon Cascade Mountains during the Improvement of Microphysical Parameterization through Observational Verification Experiment 2 (IMPROVE-2; November–December 2001) and over the Alps in the Mesoscale Alpine Program (MAP; September–November 1999).

Polarimetric scanning and vertically pointing S-band Doppler radar data suggest that turbulence contributed to the orographic enhancement of the precipitation associated with fronts passing over the mountain barriers. Cells of strong upward air motion (>2 m s^{-1}) occurred in a layer just above the melting layer while the frontal precipitation systems passed over the mountain ranges. Upstream flow appeared to be generally stable except for some weak conditional instability at low levels in the two IMPROVE-2 cases.

The cells occurred in a layer of strong shear at the top of a low-level layer of apparently retarded or blocked flow (shown by Doppler radial velocity data). The shear apparently provided a favorable environment for the turbulent cells to develop. The updraft cells appeared at the times and locations where the shear was strongest ($>\sim 10$ m s^{-1} km^{-1}). The Richardson number was slightly less than 0.25 at the level where the cells were observed, suggesting shear-generated turbulence could have been the origin of the updraft cells. Another possibility is that the rough mountainous lower boundary could have triggered buoyancy oscillations within the stable, sheared flow. The existence of turbulent cells made possible a precipitation growth mechanism that would not have been present in a laminar upslope flow.

The turbulent cells appeared to facilitate the rapid growth and fallout of condensate generated over the lower windward slopes of the mountains. In a laminar flow over terrain, upward motions would be unlikely to produce liquid water contents adequate to increase the density (and hence the fall speed) of precipitating ice particles by riming. The turbulent updraft cells apparently create pockets of higher values of liquid water content embedded in the widespread frontal cloud system, and snow particles falling from the parent cloud systems can then rapidly rime within the cells and fall out. Observations by polarimetric radar and direct aircraft sampling indicate the occurrence of rimed aggregate snowflakes and/or graupel in the turbulent layer. Inasmuch as the shear layer is the consequence of retardation or blocking of the low-level cross-barrier flow, and the turbulence is a response to the shear, the shear-induced cellularity is an indirect response of the flow to the topography. The turbulence embodied in this orographically induced cellularity allows a quick response of the precipitation fallout to the orography since aggregation and riming of ice particles in the turbulent layer produce heavier, more rapidly falling precipitation particles. Without the turbulent cells, condensate would more likely be advected farther up and perhaps even over the mountain range.

Small-scale cellularity has traditionally been associated with the release of buoyant instability by the upslope flow. Our results suggest that cellularity may be achieved even if buoyant instability is weak or nonexistent, so that even a stable flow has the capacity to form cells that will enhance the precipitation fallout over the windward slopes.

1. Introduction

Mountain meteorologists have long recognized that when a deep, moist layer of air rises over a mountain barrier, precipitation amounts increase sharply with distance up the slope to a certain elevation, above which the amounts then decrease (Hill 1881; Hann 1902; Henry 1902; Reed and Kincer 1917; Henry 1919; Peck and Brown 1962; Frei and Schaer 1998). The increase on the lower slopes often seems surprisingly sharp since condensed moisture requires time to accumulate on particles and make them heavy enough to fall out. Smith (1979) noted that, according to the lit-

---

Corresponding author address: Professor R. A. Houze Jr., Box 351640, Dept. of Atmospheric Sciences, University of Washington, Seattle, WA 98195-1640.
E-mail: houze@atmos.washington.edu

erature, 70%–100% of the water condensed on the windward slope fell out there (as opposed to being carried over the crest of the mountain barrier), and he wondered how the water condensed in the large-scale orographic lifting of a deep, warm, moist air current could fall out so quickly. Since microphysical processes control the growth rate of precipitation particles, the answer to this question must be a matter of determining how the microphysical processes are invigorated to accelerate the growth of precipitation particles in the upslope flow and thus produce quick and efficient enhancement of the precipitation in windward-side flow.

The microphysical processes that could speed up the fallout of hydrometeor mass on the windward side of a mountain range include coalescence, riming, and aggregation. Coalescence and riming increase the fall speeds of particles directly. Aggregation has a more indirect effect. It does not increase the overall mass of precipitation. Rather, it makes bigger particles, which form larger targets for riming. The riming increases the mass of the precipitation and results in large rimed aggregates and/or small graupel particles. This sequence speeds up the fallout of precipitation since the rimed aggregates and graupel fall out faster than unrimed snow. In addition, when the large aggregates melt, they become large, rapidly falling raindrops, which can in turn collect cloud droplets. We will focus primarily on the processes affecting the fallout of ice particles above and within the melting layer. Whatever mechanism enhances the fallout of ice hydrometeor mass on the windward side must favor riming and/or aggregation combined with riming.

In this paper, we examine the orographic enhancement of deep precipitating frontal cloud systems that move over mountain ranges. In such cloud systems, precipitation forms primarily by the classic stratiform process: over a broad region of gentle ascent of air, ice particles aloft grow by deposition, drift downward slowly, aggregate to form larger snow particles, and melt to form raindrops (Houze 1993, chapter 6). The fallout of the ice particles and raindrops in such a cloud system can be accelerated if cellular air motions occur within the precipitating cloud layer (Smith 1979). If the cellular motions exist above the 0°C level, they may promote aggregation by creating a field of highly variable and turbulent air motions, which make it easier for ice particles to collide with each other. In addition to promoting ice particle collisions and aggregation, the updrafts of the cells promote coalescence and riming by producing small-scale pockets of higher cloud liquid water content. If the cells are located above the 0°C level and produce supercooled droplets in these pockets, the preexisting ice particles of the frontal cloud, which have been aggregating in the field of turbulent air motion, will rapidly accrete the supercooled water. Thus, they will turn into rimed aggregates or graupel and fall out more rapidly than they would as unrimed aggregate snow particles.

A moist layer rising over a mountain may break down into a cellular substructure if the layer has a potentially unstable stratification. If the moist layer approaching the barrier is absolutely stable, one might not expect cellularity. However, we will describe cases of frontal cloud systems in which strong cellularity occurred in stable or nearly stable flow impinging on a mountain range. The cellularity in these cases appears to have arisen in the form of turbulence owing to the manner in which the stable airflow reacts to the mountain barrier. Two of the storms we describe moved from the Pacific Ocean over the lower slopes of the Cascade Mountains of Oregon during the Improvement of Microphysical Parameterization through Observational Verification Experiment 2 (IMPROVE-2; Stoelinga et al. 2003). A third case occurred during the Mesoscale Alpine Program (MAP; Bougeault et al. 2001) as a baroclinic system approached the Alps. We will describe the embedded cells that occurred in these storms, determine the probable origin of the cellularity, and examine the role of the cellularity in the orographic enhancement of the frontal precipitation. The MAP case is the intensive observing period 8 (IOP8) storm, described extensively in previous papers (Rotunno and Ferretti 2003; Bousquet and Smull 2003; Medina and Houze 2003). Therefore, we will not repeat a detailed discussion of that case here. We will first discuss the IMPROVE-2 and MAP datasets (section 2). Then we will describe the two IMPROVE-2 cases in detail (section 3). Finally, we will briefly make a comparison to the MAP IOP8 case (section 4). In section 5 we will tie the results from the two regions together in a conceptual model and discuss the conclusions and implications of our results in section 6.

2. Data

Figure 1 shows the location of the observational facilities used in this study relative to the terrain and the observational areas for IMPROVE-2 and MAP. In Fig. 1a, the Cascades run approximately north–south through the experimental area. The crest is ~2 km MSL. In Fig. 1b, the Alps encircle the region of the Lago Maggiore in Italy. The crest is ~4 km MSL. The observational networks in IMPROVE-2 and MAP were similar. The National Center for Atmospheric Research (NCAR) S-band dual-polarization Doppler radar (S-Pol) was used in both MAP and IMPROVE-2 to scan over the windward slope of the mountain ranges.

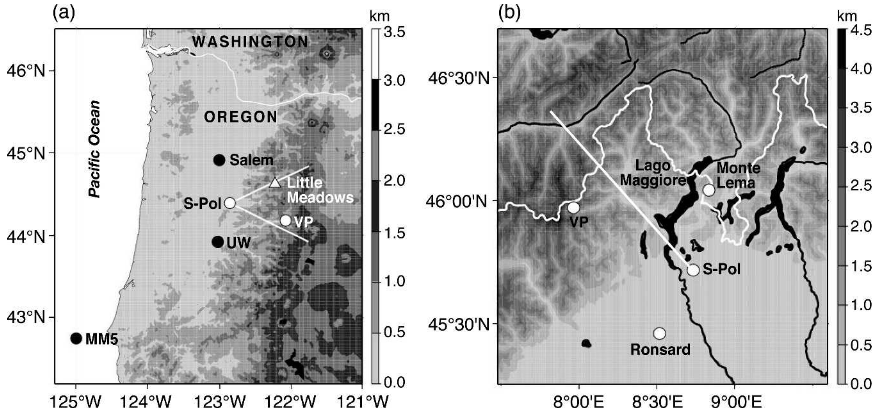

FIG. 1. (a) IMPROVE-2 observational area. Western Oregon topography is shown with the location of the observations relevant to this paper. S-Pol marks the location of the polarimetric scanning Doppler radar. The white lines bound the eastward-looking sector scanned regularly during the 13–14 Dec 2001 case. Here, VP marks the location of the vertically pointing radar. Salem and UW denote upper-air sounding locations. MM5-simulated soundings for the indicated site are also presented. Black circles denote upper-air sounding sites, white circles denote radars, and triangles denote rain gauge sites. (b) MAP observational network showing locations of the Ronsard, S-Pol, Monte Lema, and ETH (VP) radars. For further details of the MAP data network, see Medina and Houze (2003).

Vertically pointing radars were placed on the windward slopes to provide precipitation details with high resolution in time and height. The Swiss Federal Institute of Technology (ETH) vertically pointing X-band radar was operated during MAP. In IMPROVE-2, the National Oceanic and Atmospheric Administration (NOAA)/Environmental Technology Laboratory (ETL) vertically pointing S-band Doppler radar was deployed (White et al. 2000). Characteristics of the radars are listed in Table 1.

When precipitation was occurring close to or over the experimental area, the S-Pol radar scanning sequence in IMPROVE-2 consisted of the following:

(i) surveillance plan position indicator (PPI) scans collected normally at 0.5°, 1.5°, and 2.4° of elevation;
(ii) an eastward-looking sector consisting of 60 range–height indicator (RHI) scans at 1° azimuth intervals (An example of an eastward-looking sector for the 13–14 December case is shown in Fig. 1);
(iii) a westward-looking RHI.

This cycle of PPIs and RHIs required ~11 min to complete. In MAP, the S-Pol scanning sequence consisted of azimuthal sector scans manually adjusted to cover the region of heaviest orographic precipitation. The S-Pol scans alternated PPI sectors with RHI sectors.

A radar scanning over a mountain range (Fig. 1) receives data contaminated by returns from the terrain. Ground-clutter contamination was removed from the S-Pol MAP and IMPROVE-2 datasets by the following two-step process:

(i) Time-independent part: A three-dimensional clutter map was constructed by finding clear air scans (i.e., scans when the S-Pol radar collected data but no meteorological echo was present). Then we

TABLE 1. Radar characteristics.

Radar	Elevation of radar (km)	Peak power (kW)	Wavelength (cm)	Beamwidth (°)	Nyquist interval (m s^{-1})
NCAR/S-Pol polarimetric Doppler radar	0.475 (IMPROVE-2) 0.280 (MAP)	400	10.6	0.92	(−22.4, 22.4)
NOAA/ETL S-band vertically pointing Doppler radar	0.512	0.360	10.4	2.5	(−10.5, 10.5) for 700-ns pulse length
ETH X-band vertically pointing Doppler radar	1.3	90	3.2	2.4	(−32.0, 32.0)

made the assumption that all the reflectivity echoes greater than a threshold were due to the terrain. A value of -6 dBZ was found to be a reasonable threshold. The areas covered by echo >-6 dBZ in the clear air scans were assumed to be cluttered at all times.

(ii) Time-dependent part: The amount of ground clutter is sensitive to changes in the index of refraction of the atmosphere; therefore, it changes with time. Ground clutter was identified for each individual scan using the particle identification (PID) algorithm described by Vivekanandan et al. (1999), which is based on radial velocity statistics and polarimetric variables.

If an individual pixel were collocated with a pixel in the time-independent clutter map or if it was identified as ground clutter by the PID algorithm, then this pixel was eliminated.

After removing ground-clutter-contaminated signals, the radial velocity was unfolded using NCAR's SOLO software (Oye et al. 1995) implementation of the Bargen and Brown (1980) unfolding algorithm.

The vertically pointing NOAA/ETL S-band radar obtained data with very high temporal resolution (every 3–8 s). The radar rays were emitted alternately with pulse lengths of 300 ns (range resolution of 45 m, maximum range ~3.8 km) and 700 ns (range resolution of 105 m, maximum range 9.8 km). The former emphasized high-resolution data at lower altitudes. The latter emphasized data through a deeper layer, with less resolution at low altitudes. In this study we will make use of the 700-ns data since we are interested in the processes in a layer extending well above the 0°C level (~2 km) in the investigated storms. The ETH radar in MAP had a time resolution of 30 s.

Collocated with the vertically profiling radar (VP) in IMPROVE-2 was a NOAA/ETL wind profiler (McKenzie Bridge location). Figure 1 shows that rawinsonde soundings were taken at Salem, Oregon, as well as at a University of Washington (UW) mobile sounding site at the foot of the mountain range. In addition, model output from a nudged version of the fifth-generation Pennsylvania State University–NCAR Mesoscale Model (MM5; Garvert et al. 2005) provided upstream soundings at the indicated site in Fig. 1.

For the IMPROVE-2 cases we examine ice particle images obtained in the frontal cloud layer with the Knollenberg Particle Measuring System (PMS) probes on a NOAA WP-3D aircraft. We also refer to the flight-level meteorological parameters measured aboard the aircraft. Unless otherwise stated, all the altitudes in this paper are MSL.

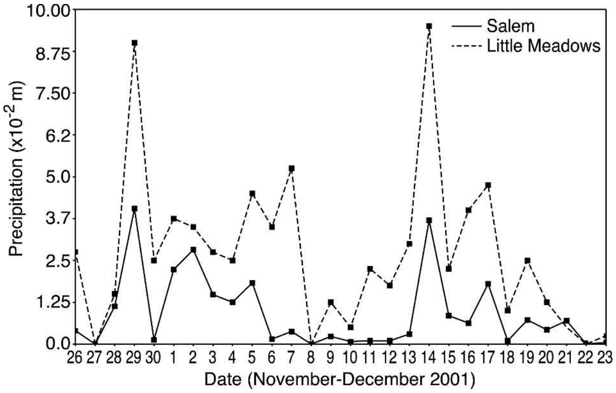

FIG. 2. IMPROVE-2 time series of daily precipitation according to Salem and Little Meadows rain gauges.

3. Description of the IMPROVE-2 cases

a. Observed precipitation enhancement

During the entire time period of IMPROVE-2 (26 November–22 December 2001), westerly flow persisted in the lower troposphere, and 16 short-wave troughs came across the region with associated frontal cloud systems. Precipitation gauge data from two sites illustrate the orographic enhancement of the precipitation falling from these storms on the lower windward slopes of the Oregon Cascades (Fig. 2). Salem is in the lowland region upwind of the Cascades, while Little Meadows lies about halfway up the slope, ~70 km southeast of Salem (Fig. 1). The amount of precipitation accumulated during IMPROVE-2 was 0.259 m in Salem compared to 0.775 m in Little Meadows, that is, the precipitation at the windward slope station exceeded the amount of the upstream station by about a factor of 3. Each storm individually exhibited a similar increase between the two stations (Fig. 2). This result is an example of the sudden enhancement of precipitation that can occur as soon as the moist layer in the storm system begins rising over the terrain.

b. Large-scale conditions

Figure 3a shows one of the ~16 short-wave troughs that affected Oregon during IMPROVE-2. A strong southwesterly jet was over the coastline, and a front was moving in from the Pacific Ocean at 0000 UTC 14 December 2001. Figure 4a shows the frontal cloud system associated with this jet. The coldest cloud top was near the leading portion of the cloud shield, with cloud-top temperature increasing toward the back edge, which was sharply defined. This slope of cloud top (highest altitude toward the east) is consistent with the typical warm occluded structure of fronts moving in from the

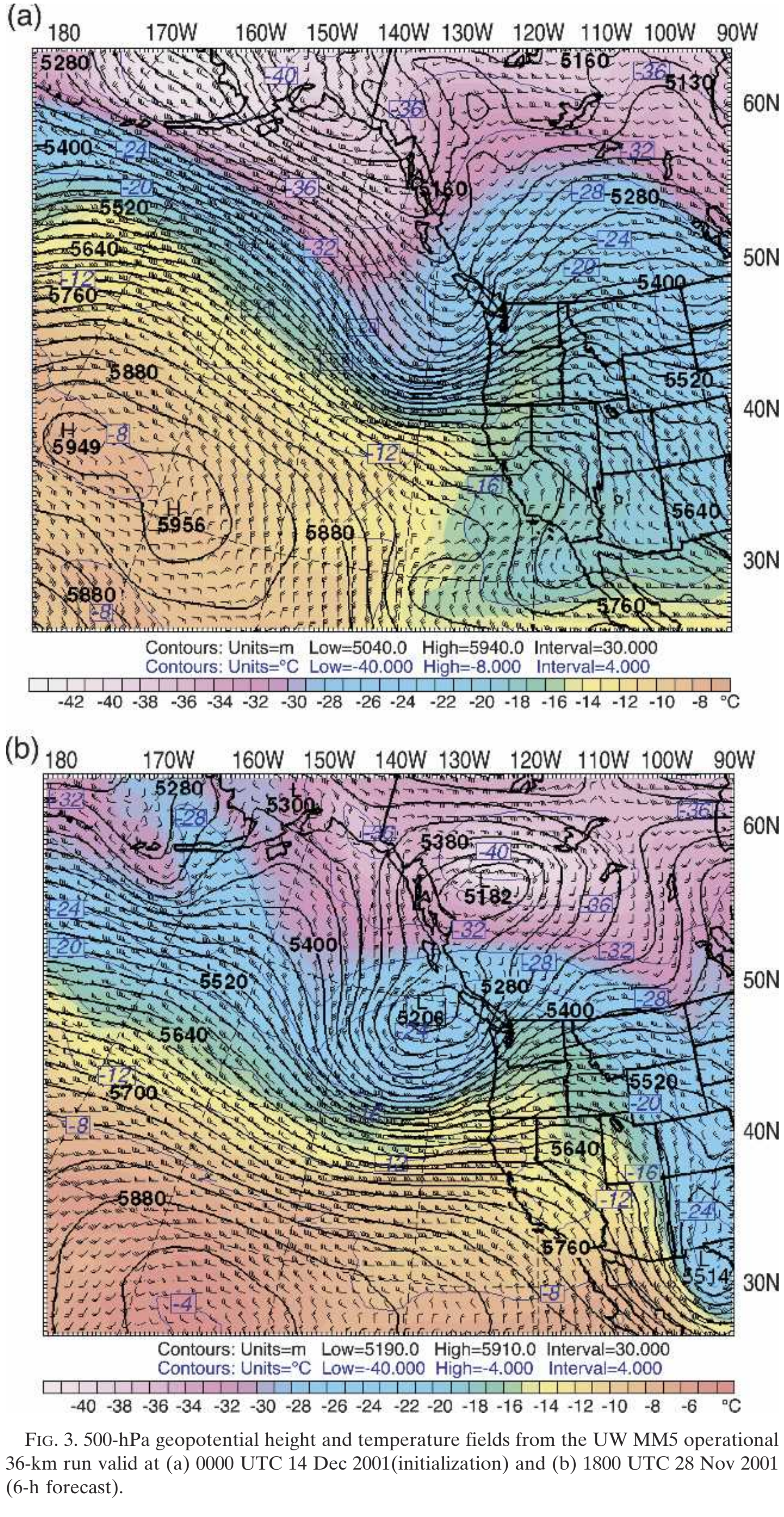

FIG. 3. 500-hPa geopotential height and temperature fields from the UW MM5 operational 36-km run valid at (a) 0000 UTC 14 Dec 2001(initialization) and (b) 1800 UTC 28 Nov 2001 (6-h forecast).

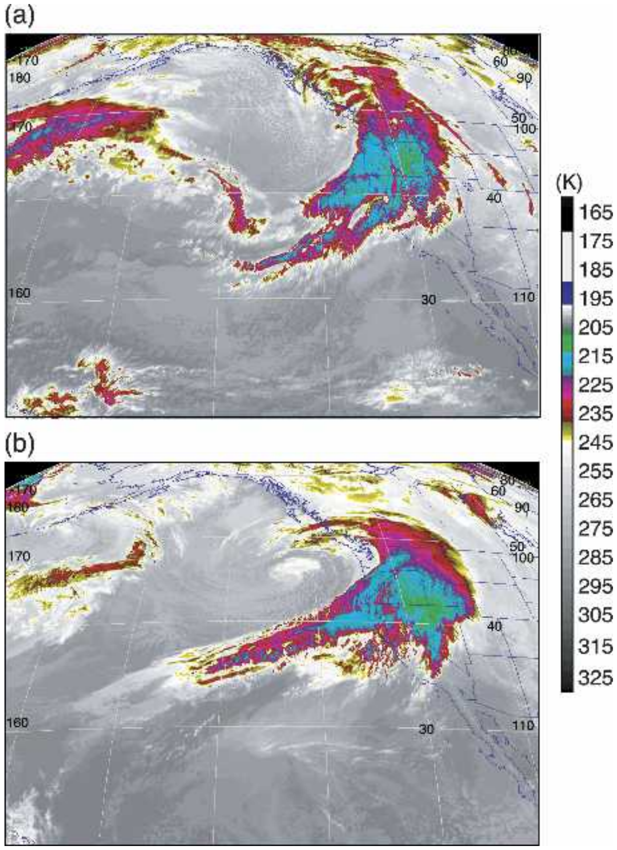

FIG. 4. Infrared satellite image at (a) 0000 UTC 14 Dec 2001 and (b) 1700 UTC 28 Nov 2001.

Pacific during the wintertime. Low-topped convective clouds were scattered throughout the trailing cold air mass over the ocean. Figure 5a shows the 0.5° elevation echo pattern on the Portland radar around 0000 UTC, when the frontal precipitation was moving over western Washington, Oregon, and northern California. The precipitation distribution associated with this storm is shown in Fig. 15a of Garvert et al. (2005) and in Fig. 16 of Woods et al. (2005). Another trough with similar extent and strength and its associated front moved from the Pacific Ocean to the western United States on 28 November 2001. The synoptic characteristics (Fig. 3b), frontal system (Fig. 4b), and radar echo (Fig. 5b) were comparable to the 13–14 December case in the experimental domain.

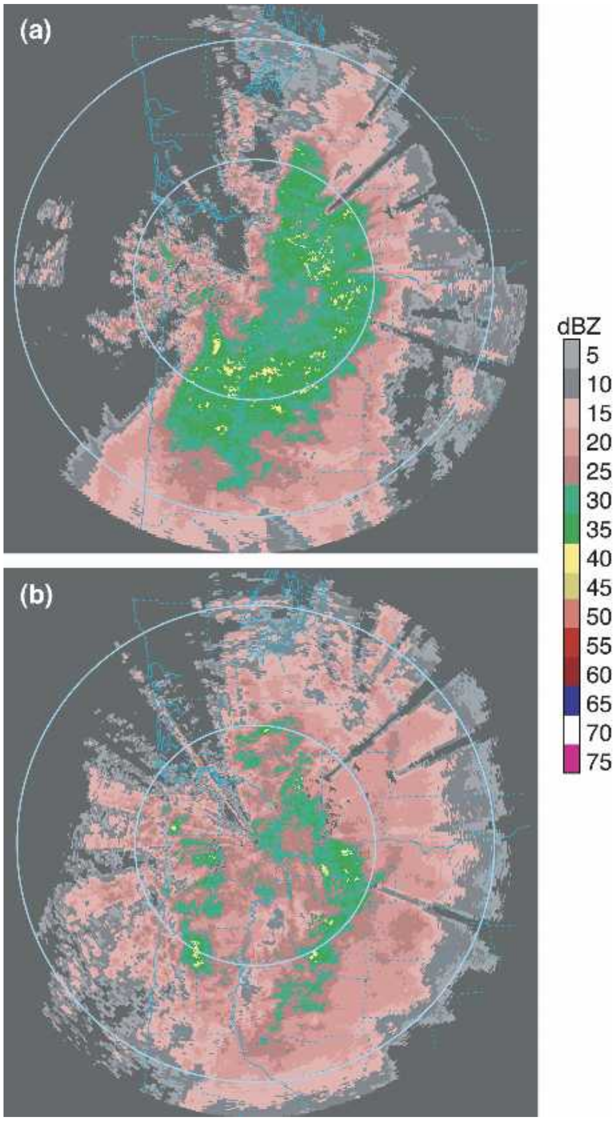

FIG. 5. The 0.5° PPI reflectivity from the Portland Weather Surveillance Radar-1988 Doppler (WSR-88D) Next Generation Weather Radar (NEXRAD) at (a) 2338 UTC 13 Dec 2001 and (b) 1653 UTC 28 Nov 2001. The range ring spacing is 100 km.

For the 13–14 December case, upstream soundings showed a stable stratification. The squared moist buoyancy frequency (N_m^2, as defined by Durran and Klemp 1982) immediately upstream of the Cascades was positive below 550 hPa for the Salem sounding at 0000 UTC 14 December, as well as farther upstream, as shown by MM5 soundings at 2200 and 2300 UTC 13 December (Fig. 6a, locations of sounding sites are in Fig. 1). For the 28–29 November case, the relevant Salem soundings also revealed stable stratification below 550 hPa (Fig. 6b). There was some slight potential instability at the base of some soundings in Fig. 6. However, it will be shown in the next section that the cross-barrier wind component of the low-level air seen on radar was very weak, apparently having suffered some retardation effect associated with its approach to the mountain range. Special soundings were collected closer to the barrier and more directly upstream of the radar-sampled region (UW location in Fig. 1a). These showed that for the 13–14 December case, N_m^2 was greater than zero (stable) from 1.8 to 4.5 km (Fig. 7a). The 28–29 No-

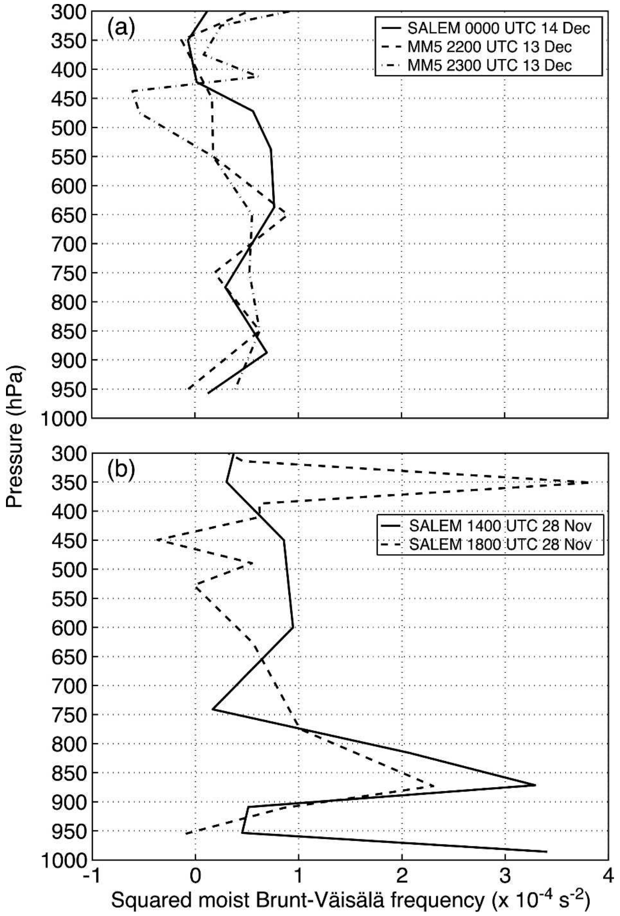

FIG. 6. Vertical profiles of squared moist Brunt–Väisälä frequency calculated from (a) Salem sounding at 0000 UTC 14 Dec 2001 and from MM5-simulated soundings at the site shown in Fig. 1a at 2200 and 2300 UTC 13 Dec 2001. (b) Salem soundings at 1400 and 1800 UTC 28 Nov 2001.

vember event showed a stable atmosphere from 0.6 to 4.5 km (Fig. 7d). At lower levels N_m^2 was close to zero or slightly negative. The vertical profile of zonal wind (i.e., cross-barrier flow, considering the Cascades have a north–south orientation) showed a maximum around 2.5 km or slightly above for both cases (solid lines in Figs. 7b,e).

c. *Evidence of a shear layer*

The cross-barrier component of the flow suggests that the air upstream of the Cascades was very weak or even negative close to the surface and it increased rapidly with height to reach a maximum of 35 m s^{-1} or more at around 2.5 km during the two storms under investigation (solid lines in Figs. 7b,e). A highly sheared layer thus was located at low levels. The shear layer is further indicated by the S-Pol radar Doppler radial velocity data averaged over the 3-h period of the frontal precipitation passage over the windward slope of the Cascades (Figs. 8a,b and 9a,b). These cross sections extend from the S-Pol radar toward the crest of the mountains. The radial velocity patterns suggest weak flow close to the terrain. The weak flow near the surface over the foothills is consistent with air being slowed down by the mountain barrier. A layer of strong shear bounds the top of the layer of apparently retarded or partially blocked flow. The shear layer is observed by the S-Pol radar to only about a 60-km range, or about halfway up the mountain barrier, possibly because of the widening of the beam at farther ranges and beam blockage by the terrain. This velocity signature is discussed in more detail by Medina et al. (2005). This radial velocity signature of a retarded low-level flow contrasts with unblocked orographic flow, which exhibits a radial-velocity jet rising up and over the first major rise of terrain (e.g., Fig. 12b of Medina and Houze 2003).

d. *Precipitation processes indicated by polarimetric radar*

The radar reflectivity averaged over the 3-h passage of the frontal rainband (in each storm) shows a well-defined bright band over the lower windward slopes of the Cascades in the region of the radar volume that was not shielded from view by the mountains nearest the S-Pol radar (Figs. 8c,d and 9c,d). The bright band is a signature of the stratiform precipitation process. The general nature of the processes contributing to the formation of the bright band have been known for over 50 years (Austin and Bemis 1950; Battan 1973). The basic sequence of events as ice particles fall from above the 0°C level to levels below in a stratiform precipitating cloud are summarized by Houze (1993, chapter 6) and Houze (1997). In a quasi-steady, deep, horizontally uniform nimbostratus cloud, precipitating ice particles initiated in upper (subfreezing) levels aggregate as pass through temperatures of $-10°$ to $-15°$C and even more so at temperatures of $-5°$ to 0°C (Hobbs 1974). Since the aggregation processes produce a large increase in particle size, the aggregate snowflakes increase the radar reflectivity, which is proportional to the sixth power of the diameter, just above the melting layer. When the particles fall below the 0°C level, they may continue to aggregate and increase in reflectivity, and as the aggregates begin to melt, their reflectivity is further enhanced by changes in the dielectric constant, which make the index of refraction of the aggregates more like that of liquid (Austin and Bemis 1950; Willis and Heymsfield 1989). Fabry and Zawadzki (1995) have evaluated the relative effects of nonsphericity of melt-

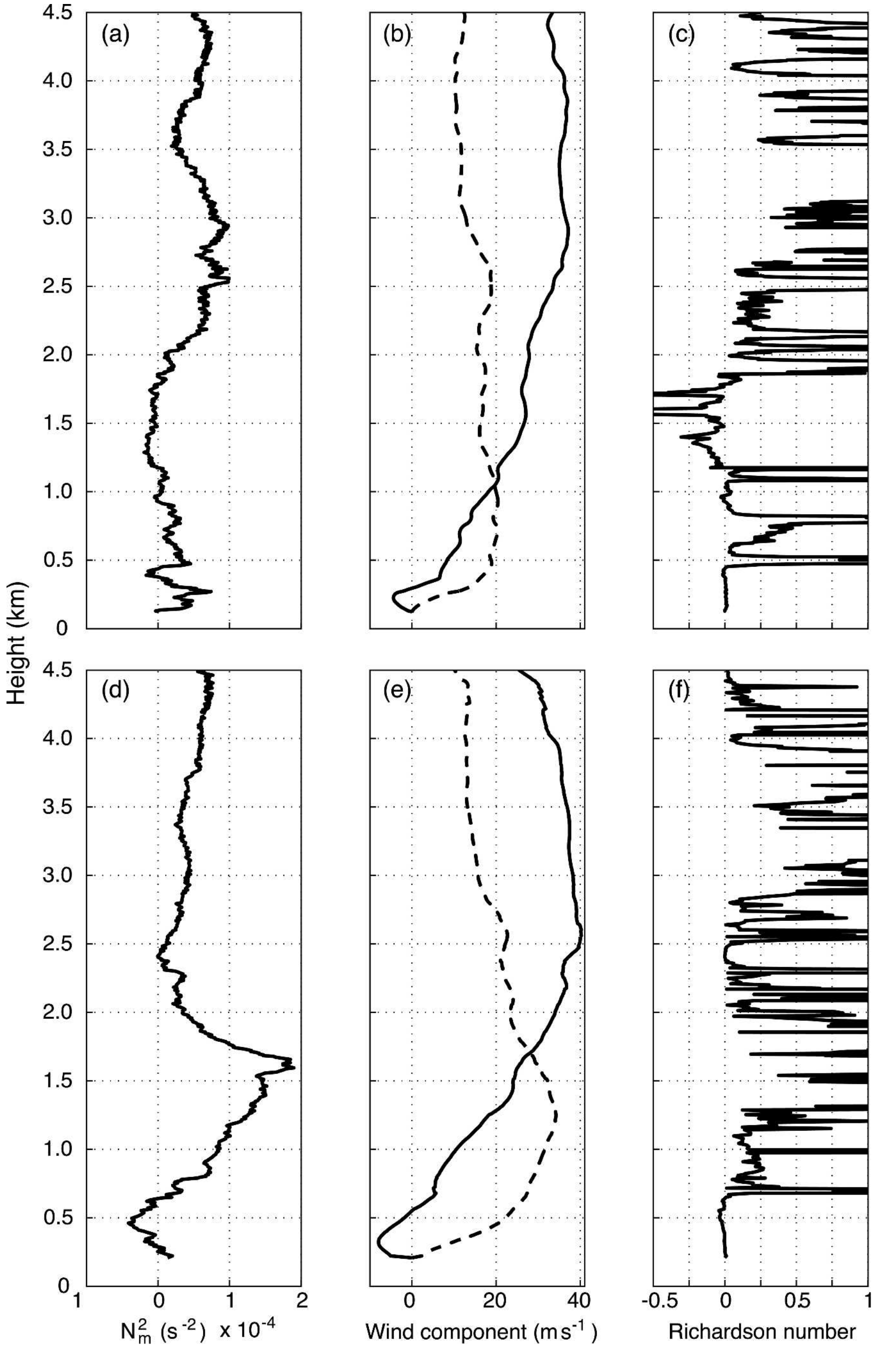

FIG. 7. Vertical profiles according to UW sounding of (a) squared moist Brunt–Väisälä frequency, (b) zonal (solid line), and meridional (dashed line) components of the wind, and (c) Richardson number at 2356 UTC 13 Dec 2001. (d)–(f) Same as (a)–(c) except for 1726 UTC 28 Nov 2001.

ing hydrometers and the way water is distributed within the melting snowflake and found that the relative contribution of each process to the brightband intensity is rain-rate dependent. The reflectivity suddenly drops off when the aggregates completely melt and collapse into rapidly falling raindrops. There is also evidence of breakup effects being important when the rain rate is sufficiently high (Drummond et al. 1996).

Since the reflectivity patterns in Figs. 8 and 9 are compilations of the data collected over 3-h intervals,

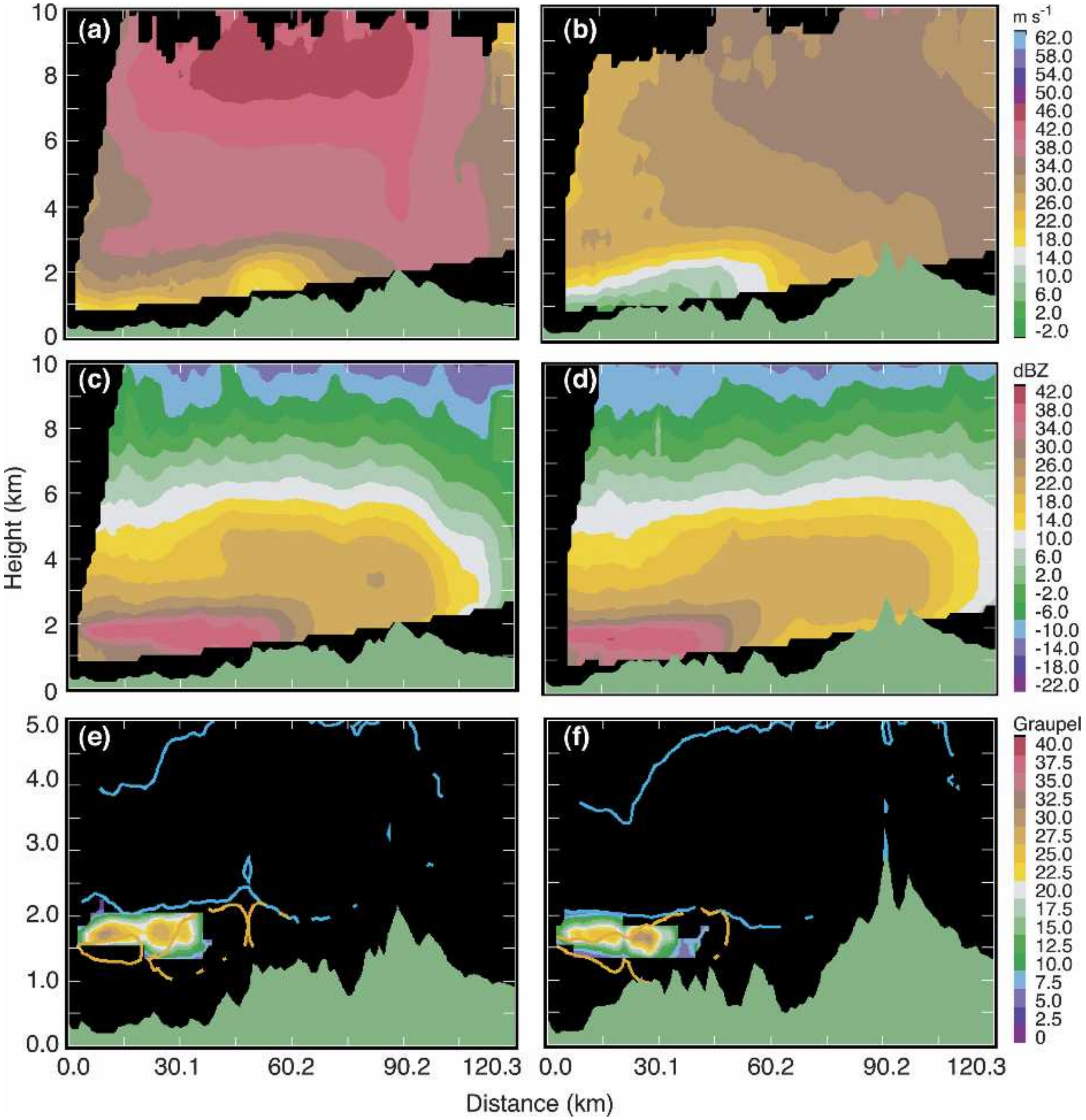

Fig. 8. Vertical cross section of NCAR S-Pol radar data extending from the radar site, located on the lower-left corner of the panels, across the Cascade Range (a), (c), (e) to the east-northeast (70°) and (b), (d), (f) to the east-southeast (110°). The topography is shown in the lower part of each panel. The fields have been either averaged or accumulated over a 3-h period, from 2300 UTC 13 Dec–0200 UTC 14 Dec 2001. (a), (b) Mean radial velocity, with positive (negative) values denoting flow away from (toward) the radar. (c), (d) Mean reflectivity. (e), (f) Frequency of occurrence of particle types: 60% of snow (cyan), 35% of melting aggregates (orange), and graupel or dry aggregates (shading).

details of the precipitation processes operating at any given time are obscured. To indicate the processes that were occurring in the mean bright band, we examine the radar echo cross section at a single representative time. Figure 10 includes information gained from the polarimetric variables measured by the S-Pol radar at 2100 UTC 13 December 2001.

Figure 10a contains the horizontally transmitted/horizontally received equivalent radar reflectivity factor (Z). This quantity is the conventional reflectivity, as

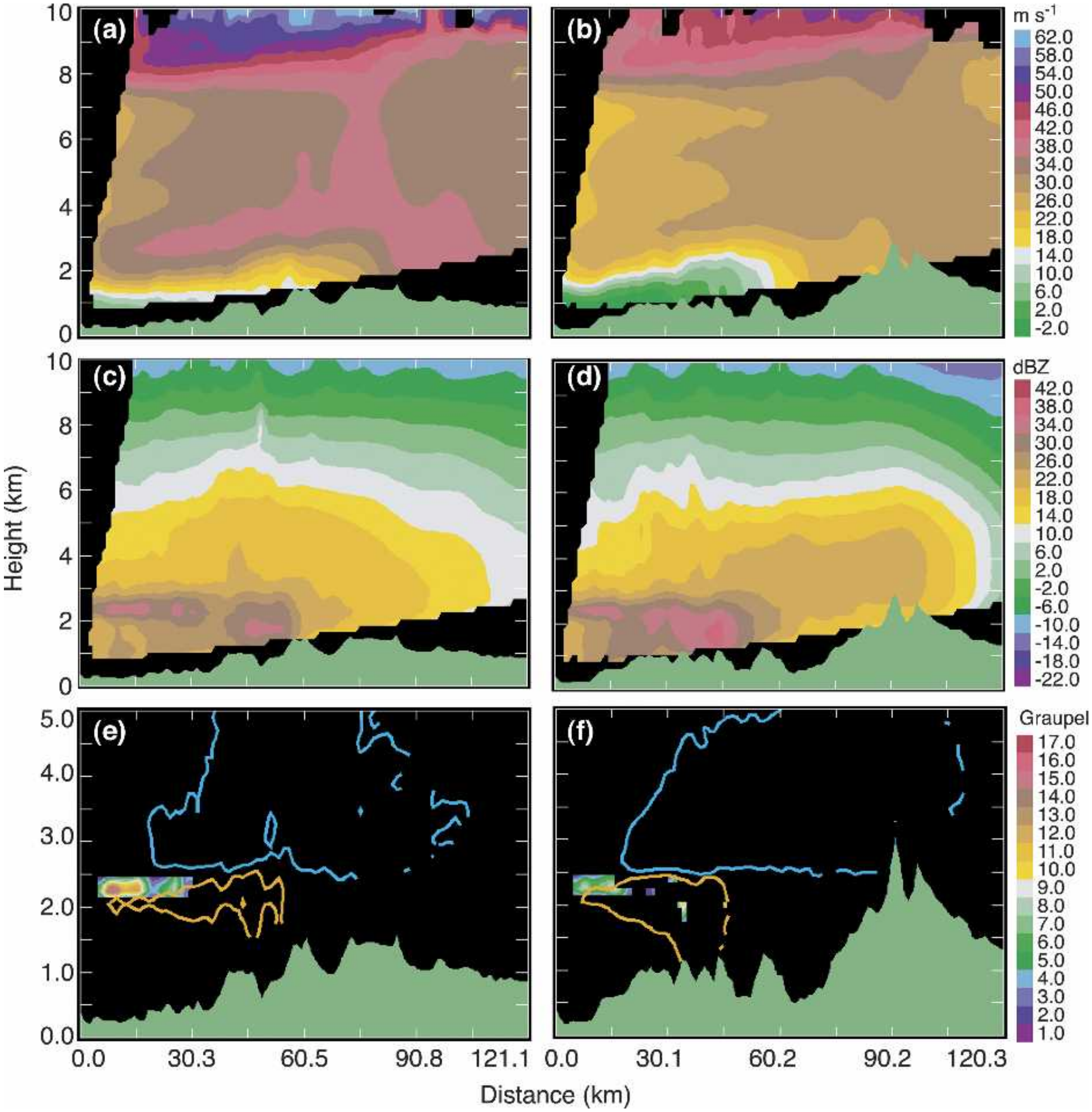

FIG. 9. Vertical cross section of NCAR S-Pol radar data extending from the radar site, located on the lower-left corner of the panels, across the Cascade Range (a), (c), (e) to the east (90°) and (b), (d), (f) to the east-southeast (110°). The topography is shown in the lower part of each panel. The fields have been either averaged or accumulated over a 3-h period, from 1600–1900 UTC 28 Nov 2001. (a), (b) Mean radial velocity, with positive (negative) values denoting flow away from (toward) the radar; (c), (d) mean reflectivity, (e), (f) frequency of occurrence of particle types: 60% of snow (cyan), 35% of melting aggregates (orange), and graupel or dry aggregates (shading).

provided by any ordinary meteorological radar. Figure 10b contains the differential reflectivity [ZDR $\equiv$ 10 log($Z_{\mathrm{HH}}/Z_{\mathrm{VV}}$), where Z_{HH} is the horizontally transmitted/horizontally received radar reflectivity factor and Z_{VV} is the vertically transmitted/vertically received radar reflectivity factor]. Figure 10c contains the color-coded field of hydrometeor types identified from polarimetric variables by a slightly modified version of the algorithm of Vivekanandan et al. (1999). Their algorithm incorporates measured polarimetric radar variables into an automated scheme to identify the most probable categories of precipitation particles contribut-

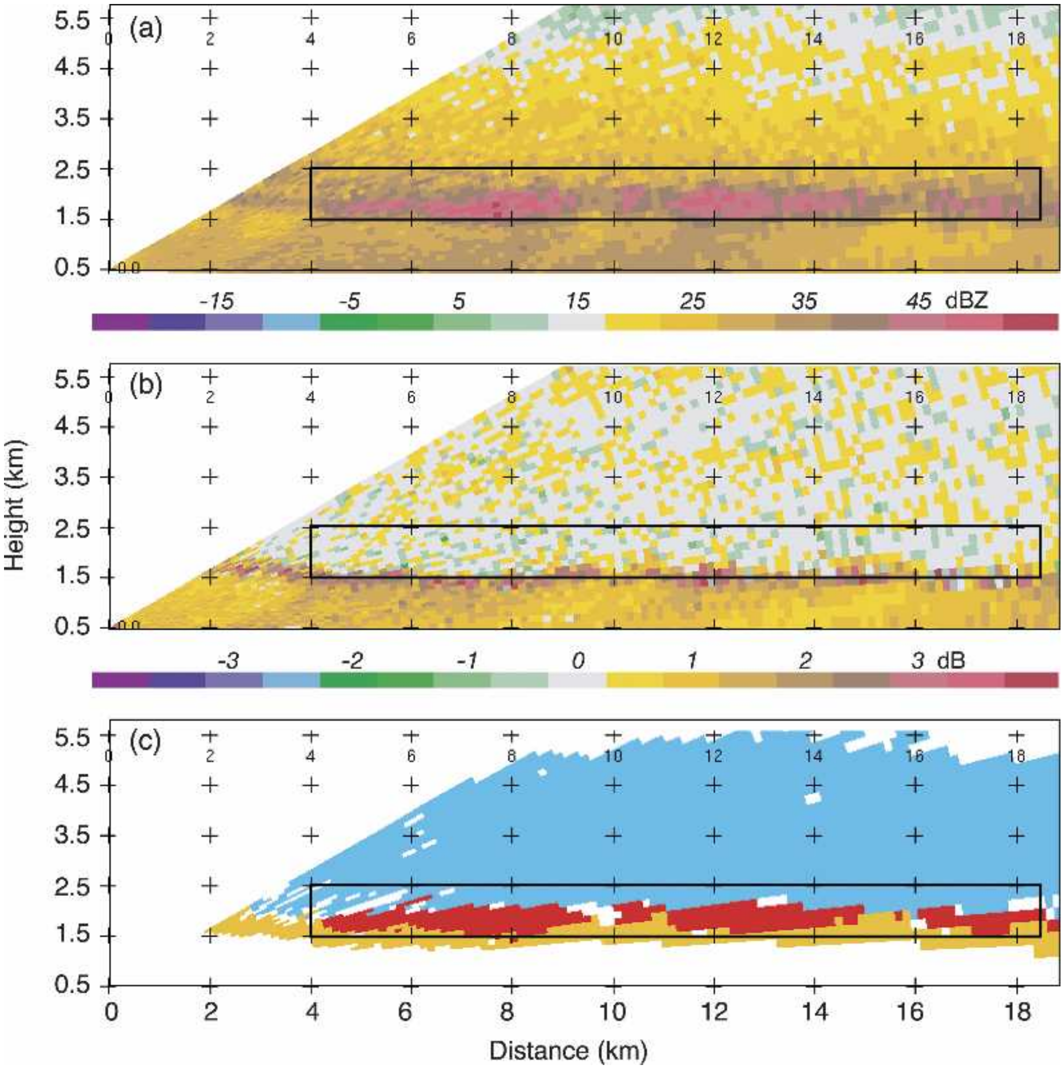

FIG. 10. NCAR S-Pol radar RHI at 2100 UTC 13 Dec 2001 for an azimuth of 80° showing (a) reflectivity, (b) differential reflectivity, and (c) particle type, where cyan pixels indicate snow, red pixels indicate graupel or dry aggregates, and orange pixels indicate melting aggregates. The black rectangles show the exact same position in (a)–(c).

ing to the radar signal. This algorithm is heavily based on three parameters: reflectivity, differential reflectivity, and temperature, though it also uses the linear depolarization ratio (LDR), specific differential propagation phase (K_{DP}), and the lag-zero correlation coefficient of horizontally and vertically polarized echoes (ρ_{hv}).[1] Zeng et al. (2001) have used a similar scheme, as have other investigators. In this study, we focus on three particle categories listed in Table 2. For purposes of this paper, we have applied a different set of names for these categories than those suggested by Vivekanandan et al. (1999; see first two columns of Table 2). Our names attempt to represent more precisely the types of particles present in the storms investigated in IMPROVE-2. The algorithm of Vivekanandan et al. (1999) grew out of investigations of convective storms (especially hailstorms) in which the microphysical processes in the ice regions are dominated by riming, with aggregation playing little if any role. In frontal systems, such as those investigated in IMPROVE-2, both aggregation and riming play important roles. Our names bring out the possible importance of aggregates in the spectrum of ice particles present in these storms.

Our renaming is as follows: 1) We change their category name dry snow simply to snow, which in our study is likely some combination of pristine crystals and

---

[1] See Straka et al. (2000) for a description of polarimetric radar variables.

TABLE 2. Ice particle categories inferred from S-Pol data in this study.

Category name used in this study	Vivekanandan et al.'s (1999) category name	Reflectivity range (dB*Z*)	Differential reflectivity (ZDR) range (dB)	LDR (dB)	K_{DP} (° km^{-1})	ρ_{hv}
Snow	Dry snow	10 to 35	−1.0 to 1.4	−28 to −21	−0.1 to ~0.2	>0.97
Melting aggregates	Wet snow	20 to 50	>0.3	−24 to ~−15	−0.05 to 1.2	0.7 to 0.98
Graupel and/or dry aggregates	Small graupel/hail	33 to 55	−3.0 to ~1.9	~−29 to ~−18	−0.2 to ~2.5	0.85 to ~1.0

aggregates at the higher levels of the frontal cloud, where ice particles are forming and growing by vapor deposition. 2) We change their category wet snow to melting aggregates, since this category exclusively appears at the base of the bright band and it is widely recognized that the bright band is associated with melting aggregates. Aircraft data (discussed below) verify the preponderance of aggregates above the melting layer in these cloud systems. 3) Most importantly, we rename their category small graupel/hail to graupel and/or dry aggregates. There is extensive literature that shows that in frontal cloud systems of the type under investigation here, hail certainly does not occur; graupel is small when it does appear, and rimed snowflakes are common (Hobbs 1975; Marwitz 1987). It is our impression that Vivekanandan et al.'s small graupel/hail category is triggered in the IMPROVE-2 storms primarily by large aggregates. This behavior of the algorithms is understandable since the distinction between large aggregates and small graupel in terms of reflectivity and differential reflectivity is probably slight. We suggest that our renaming of the category better fits this experience. The IMPROVE-2 aircraft data discussed later in this paper corroborate this impression.

Generally speaking, the three categories of particles in Table 2 are identified within the indicated ranges of polarimetric observables. The Vivekanandan et al. (1999) algorithm, however, works by fuzzy logic, which means that the given thresholds are not rigid but rather applied in a probabilistic manner. Temperature, dB*Z*, and ZDR data are heavily weighted, whereas LDR, K_{DP}, and ρ_{hv} are assigned a smaller weight. The particle categories that we consider are as follows:

(i) Snow: Defined by low reflectivity (10 to 35 dB*Z*), low ZDR (−1.0 to 1.4 dB), and (to a lesser degree) the other variables given in Table 2. These value ranges are consistent with small dry snow particles (small ice particles with random orientation and low dielectric constant). The criteria of Table 2 lead to the pattern of frequent hydrometeor types plotted in Fig. 10c. The layer between ~2 and 5.5 km is dominated by the snow category because of the low reflectivity (Fig. 10a) and low ZDR (Fig. 10b) that prevail throughout this layer.

(ii) Melting aggregates: Defined by high reflectivity (20 to 50 dB*Z*), high ZDR (>0.3 dB), and (to a lesser degree) the other variables given in Table 2. These value ranges are consistent with the largest hydrometeors being wet aggregate snowflakes (large horizontally oriented particles with high dielectric constant). The radar bright band, traditionally identified as a layer of maximum reflectivity, is associated with melting. In Fig. 10a, the bright band appears in the reflectivity field as dark brown and red. It is approximately 0.4-km thick, and does not give a very precise indication of the level at which melting occurs. The ZDR field identifies the melting level more precisely. Figure 10b shows that the values of ZDR throughout most of the depth of the reflectivity bright band in Fig. 10a were small, near zero. The vertical profile of ZDR has a very large and sudden jump at ~1.5 km, which is evidently the level at which particles begin to melt, and the largest aggregate snowflakes undergo a jump in their apparent dielectric constant, which magnifies the ZDR signal resulting from their typical horizontally oblate orientation. The categories identified by the criteria of Table 2 and plotted in Fig. 10c identify the echo layer just above the rain layer as melting aggregates because of the high reflectivity (Fig. 10a) and high ZDR (Fig. 10b) that prevail in this layer.

(iii) Graupel and/or dry aggregates: Defined by high reflectivity (33–55 dB*Z*), low ZDR (−3.0 to ~1.9 dB), and (to a lesser degree) the other variables given in Table 2. Graupel is known to be characterized by high reflectivity and low ZDR. The high reflectivity of graupel arises because the particles may be large and/or dense. The low ZDR of graupel arises because the particles do not exhibit highly preferred orientations (Wakimoto and Bringi 1988), and they have a low dielectric constant (Straka et al. 2000). The sudden jump in ZDR in Fig. 10b and the reflectivity bright band throughout most of its depth was occupied by dry particles, whose melting had either not yet begun or had not yet made the particles appear wet to the radar. The sudden jump in ZDR, as noted above, was in any case a strong indication that aggregates were present just above the 0°C level but only became apparent in the ZDR field when they began to melt and experienced a sharp increase in dielectric constant by becoming wet. Bader et al. (1987) found dry (i.e., nonmelting) aggregates to have low ZDR; however, they examined rather light stratiform precipitation, which might not be precisely similar to that occurring in the cases we are investigating. In the IMPROVE-2 cases, the aggregates were large. The aircraft data discussed below (section 3f) indicate that aggregates were ubiquitous above the 0°C level. Many were apparently rimed. Graupel images were not highly apparent, but could not be ruled out. It is possible that large dry aggregates (including rimed aggregates) dominated the high-reflectivity values seen in the layer above the 0°C level (Fig. 10a) but retained a low value of ZDR (Fig. 10b, in the layer above the sharp jump) as long as they remained dry, with a low dielectric constant. To account for this possibility, Fig. 10c indicates the hydrometeor types in the layer sandwiched between the snow aloft and the melting aggregates below as graupel and/or dry aggregates.

(iv) Rain: The moderate values of Z and ZDR seen below the bright band in Figs. 10a,b, respectively, are indicated simply as rain by the polarimetric algorithm (not shown in Fig. 10c).

To determine if the processes indicated by polarimetry in Fig. 10c apply broadly in time and space in this storm, we have applied the method of Vivekanandan et al. (1999) to the S-Pol radar data for the whole volume scanned during the passage of the midlatitude systems. Figures 8e,f and 9e,f show polarimetric particle-identification results for the same 3-h time period as the radial velocity and reflectivity cross sections in Figs. 8a–d and 9a–d. These cross sections show the location and frequency of occurrence of particles of types i–iii (defined previously) during the passage of the frontal precipitation system over the windward slopes of the Cascades. The polarimetric results in these cross sections indicate that the hydrometer distribution seen in Fig. 10 was common throughout the passage of the main rain area of the frontal system (Figs. 4 and 5). The composite layering was less sharp because of variability of the layering over time and because the inferred hydrometeor types were binned in regular Cartesian grid volumes of lower resolution than the original data to calculate the frequency of occurrence of each particle type. The layers of snow aloft, dry aggregates, or graupel in the center of the brightband layer, and melting aggregates underlying the bright band seen in Fig. 10 were all evident in the composite cross sections for a 3-h time period (Figs. 8e,f and 9e,f). The frequency of occurrence of snow and melting aggregates (over 35%) indicates that these features evidently extended over a wide portion of the storm. The layer of graupel and/or dry aggregates was intermittent (maximum frequency of occurrence $< 30\%$), suggesting that whichever process was producing the graupel or dry aggregates within this extensive layer was correspondingly intermittent. The melting aggregates always lie at the bottom of the graupel-or-dry aggregate layer. The picture is thus one of a widespread frontal stratiform precipitating cloud layer intermittently punctuated just above the melting level with graupel or dry aggregates. In the next section, we see evidence that the intermittently appearing graupel or dry aggregates were likely produced by embedded turbulent cells.

e. *Turbulent air motions indicated by vertically pointing S-band radar and implications for microphysical enhancement*

The VP ETL/S-band radar located on the windward slope of the Cascades (Fig. 1a) provided detailed temporal and vertical resolution in the precipitation layer. This radar was located within the region of the S-Pol cross sections discussed above (Figs. 8b,d,f and 9b,d,f). Figures 11 and 12 show a 3-h period during the 13–14 December 2001 case (Fig. 11) and the 28 November 2001 case (Fig. 12). These sections represent the passage of the frontal precipitation over the Cascades.

In Figs. 11a and 12a the bright band appears prominently just below the 2-km level, and it shows finescale variability in the form of spikes extending both above and below the bright band. A secondary maximum of reflectivity was present around 4–4.5 km. This secondary maximum at 4–4.5 km, also seen by the S-Pol radar (Figs. 8c,d and 9c,d), could have been the result of enhanced lifting over the windward slope (possibly a gravity wave response of the flow to the mountain). Alternatively, it could have been a microphysical signature in the radar reflectivity. The temperatures at the 4–4.5-km level (approximately $-13°$ to $-15°\mathrm{C}$) would have favored growth and aggregation of dendrites (Hobbs 1974; Houze 1993). Aggregates formed at these altitudes could have been large enough to produce high reflectivity (through the sixth power of the diameter factor). A third possibility is that the reflectivity maximum at 4–4.5 km could have been the result of differ-

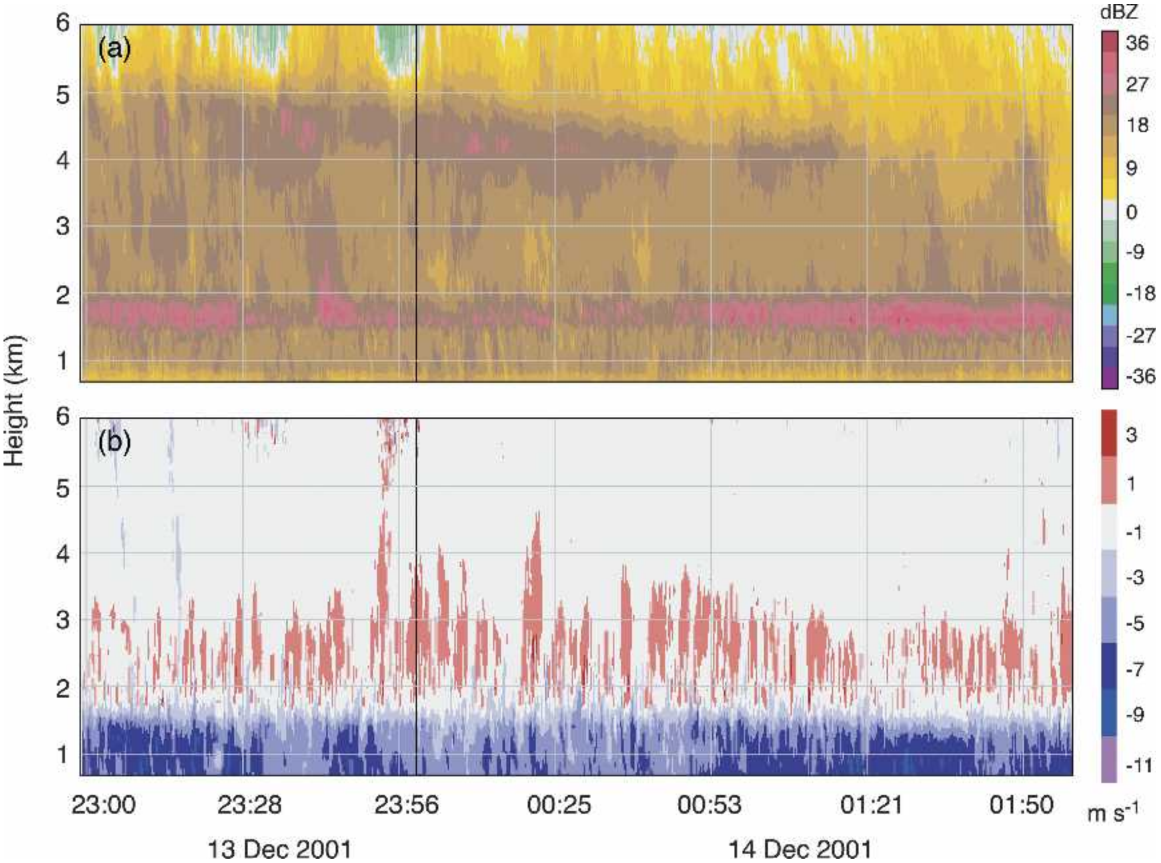

FIG. 11. Data from the NOAA/ETL S-band vertically pointing radar, located at the VP site in Fig. 1a. The data shown are for 2300 UTC 13 Dec–0200 UTC 14 Dec 2001. (a) Reflectivity and (b) radial velocity with positive (negative) values denoting flow away from (toward) the radar. The red pixels show regions where the radial velocity >0.5 m s^{-1} upward.

ential advection of hydrometeors aloft. Whatever its origin, this upper-level reflectivity maximum is not critical or even germane to the objectives of this paper.

Figures 11b and 12b show the Doppler velocity of the particles in the vertical direction. These velocities have not been adjusted for the particle fall speed in order to estimate the vertical air velocity. Thus, an upward velocity in these figures is an underestimate of the upward air motions. In the figure, we show the locations of the particles that are moving upward at 0.5 to 3.5 m s^{-1} with red shading. Since typical snow or small graupel fall speeds are 1–3 m s^{-1}, the upward air motions in these cells would be in the range of 1.5–6.5 m s^{-1} (if the antenna was truly aligned vertically so that horizontal wind was not aliased into the apparent vertical direction). Assuming the cells were being advected by winds $\sim$30 m s^{-1}, as indicated by the McKenzie wind profiler during the 3-h period under examination, we infer that the typical horizontal dimensions of the updraft cells were 1–3 km. These updrafts occurred in the layer between 2- and 3-km altitude throughout the time period of the time–height section in Figs. 11b and 12b. These updrafts probably extended vertically downward, below the 2-km level; however, melting was occurring just below the 2-km level, and the strong downward fall velocities of the raindrops would have masked the updraft air velocities in the radial velocity data.

The similarity of reflectivity and Doppler velocity patterns in Figs. 11 and 12 demonstrates that the dynamical and microphysical structures seen in the baroclinic systems passing over the Cascades have a highly repeatable behavior from one frontal system to another. An early indication of the type of vertical velocity structure seen in the IMPROVE-2 cases was provided by the Cascade Project (Hobbs 1975). In that field program, a vertically pointing Doppler radar was deployed near the crest of the Cascade Mountains of Washington (Weiss and Hobbs 1975). In one case of the passage of an occluded front over the Washington Cascade Mountains, this radar recorded updrafts $\sim$2 m s^{-1} above the melting layer, between 2- and 3-km altitude, for a period of 2 h (Hobbs et al. 1974). This radar had

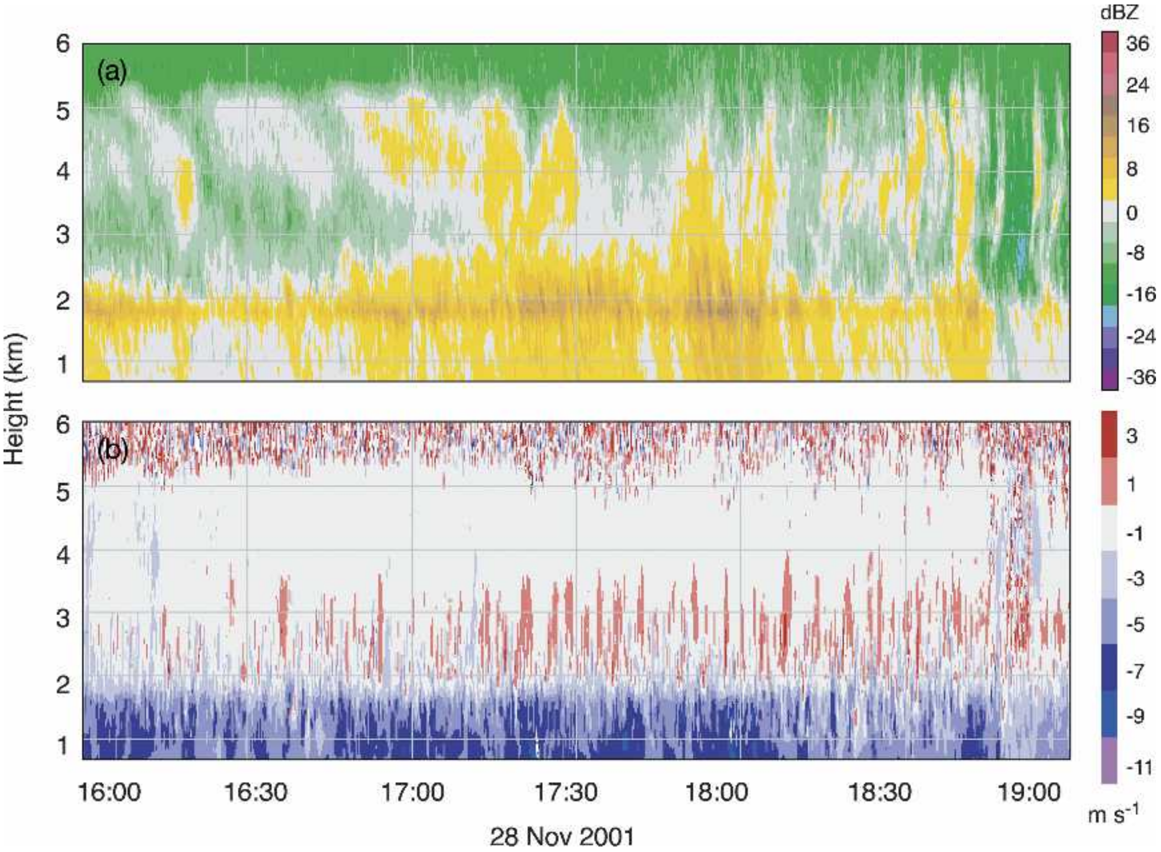

FIG. 12. As in Fig. 11, but from 1600–1900 UTC 28 Nov 2001.

rather low time resolution and did not distinguish individual cells; the comparable magnitude, duration, altitude range, and location within the frontal system were strikingly similar to the cases described in the present study.

To indicate how the radial velocity updraft cells in the two IMPROVE-2 frontal systems related both to the prevailing wind shear and to the microphysical processes, Figs. 13 and 14 compare data obtained from several sources during the passage of each storm. The period between the vertical lines corresponds to the time period shown in Figs. 8, 11, 9, and 12. Figures 13a and 14a display data from the McKenzie Bridge wind profiler. These data show how the wind shear in the 0.66–3-km MSL layer varied in time during the passage of the storm over the windward side of the Cascades. The radial velocity measured by the vertically pointing S-band radar at McKenzie Bridge is in Figs. 13b and 14b. Radial velocity updrafts of 0–6 m s^{-1} are indicated in black. Throughout the passage of the main rainband of the frontal system in each storm, the vertically pointing S-band showed the intermittent upward radial velocities seen also in Figs. 11b and 12b. Comparison of the (a) and (b) panels in Figs. 13 and 14 indicates that the radial velocity updrafts tended to occur during the period of greatest shear.

One possibility to explain the updrafts seen in Figs. 11b and 12b is that the shallow layer of weak potential instability observed below 1.5 km in the upstream flow (Figs. 7a,d) was lifted to saturation as the air ascended the Cascade Mountains and instability was released, forming a shallow layer of buoyant cells. However, the upstream instability was very weak at low levels (section 3b), and the low-level flow was weak (section 3c). The upstream air was stable in the levels where the updrafts were observed (~2–3 km). The updraft cells were therefore more likely a manifestation of some form of turbulence, induced either by the strong shear in this layer (Figs. 8 and 9) or by the flow of the stable air over the rough lower boundary formed by the windward slope terrain, or both. According to D. Durran (2003, personal communication), idealized simulations have sometimes shown that in stable flow situations a lower rough boundary can create nonstationary responses in the vertical velocity field. Hobbs et al. (1974) suggested alternatively that the updrafts they observed

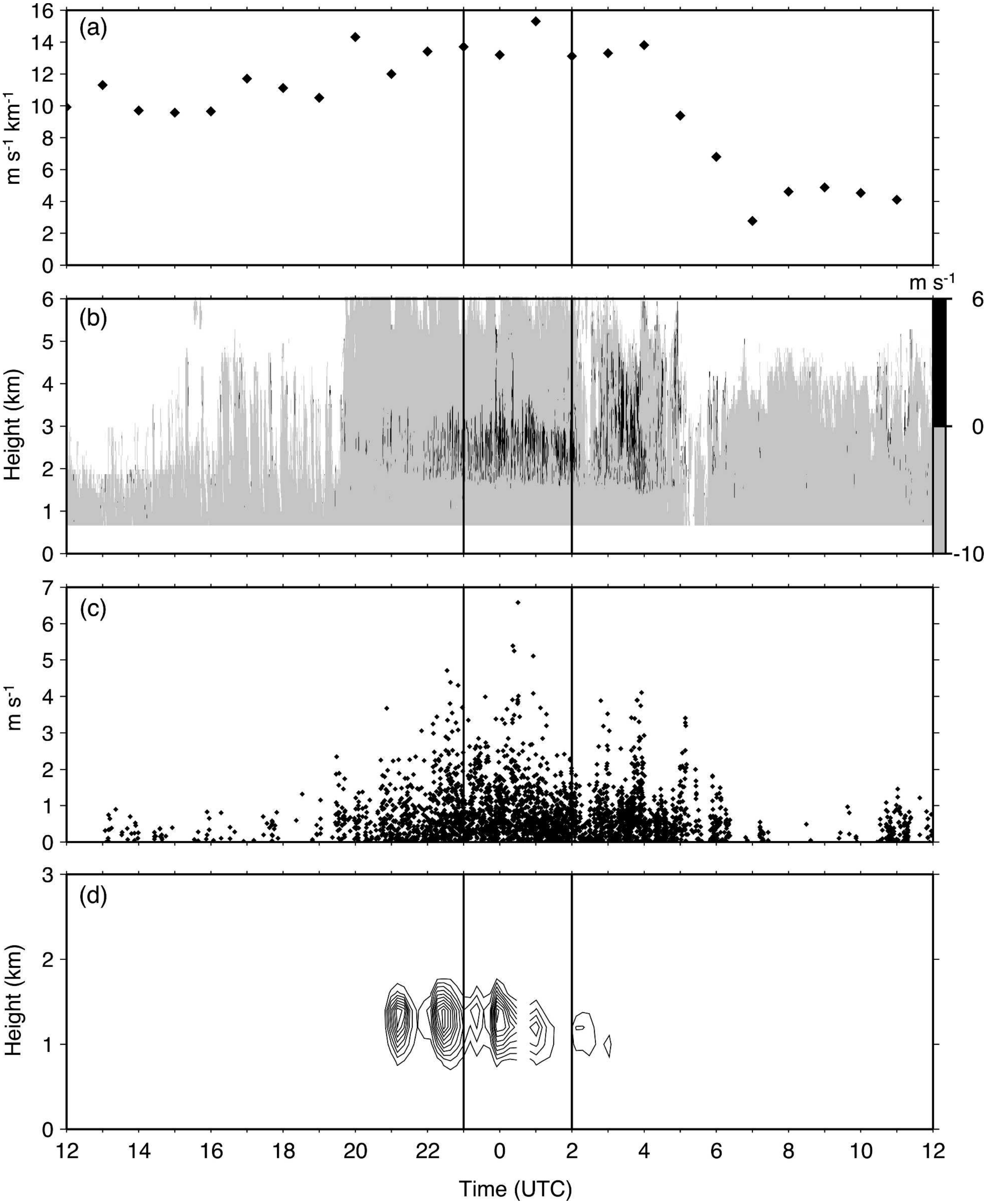

FIG. 13. Time series during the 13–14 Dec 2001 case of (a) wind shear from 0.66 to 3 km from a NOAA/ETL vertical wind profiler (McKenzie Bridge location), (b) radial velocity from the NOAA/ETL S-band vertically pointing radar, (c) maximum value of radial velocity in the 2–3-km layer from data in (b), and (d) frequency of occurrence of dry aggregates or graupel according to the microphysical particle identification algorithm described in section 3d in an eastward-looking sector from 10–60-km ranges (outer contour interval is 2%, each contour incrementing by 2%). The period between the vertical lines corresponds to the time intervals shown in Figs. 8 and 11.

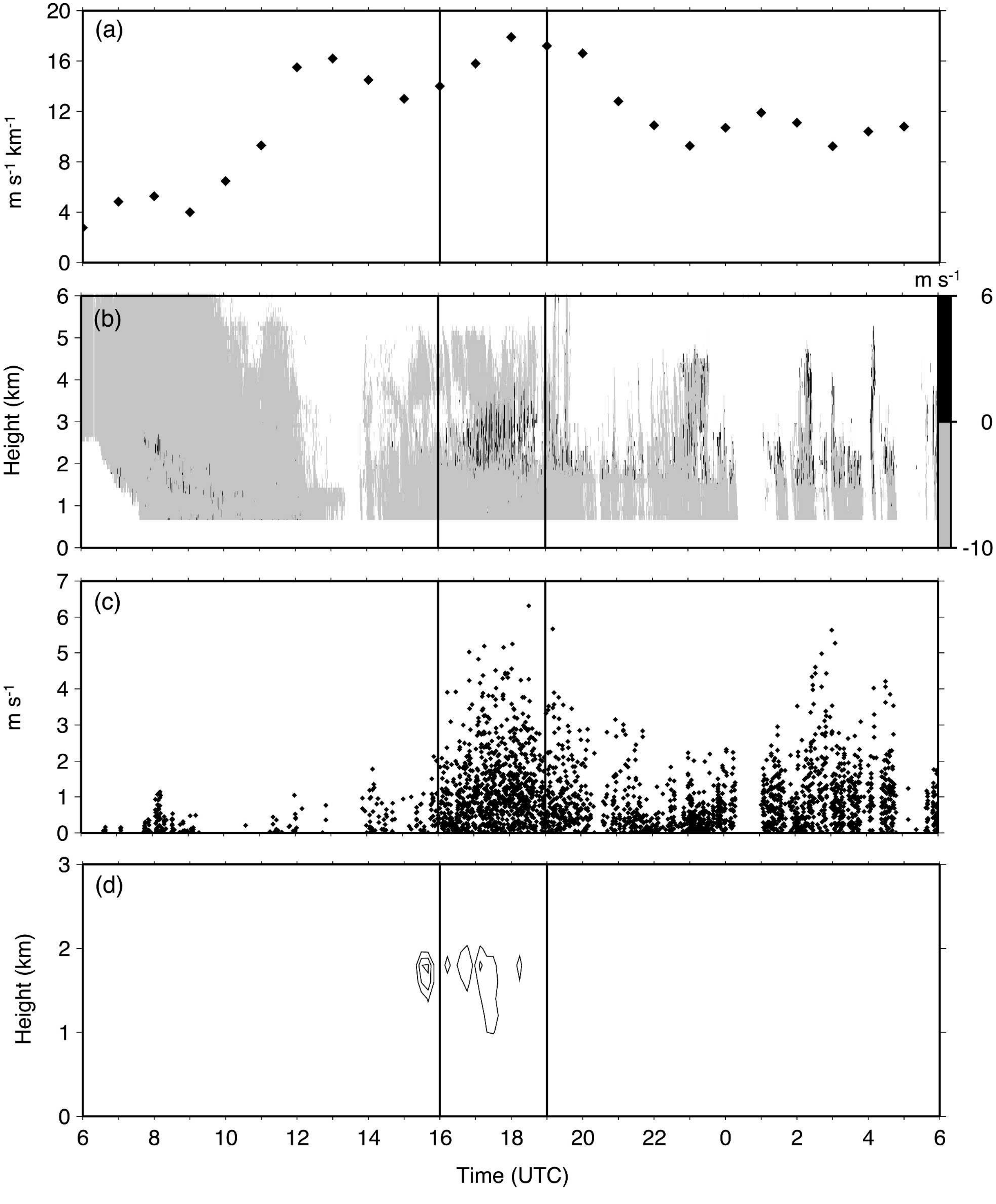

FIG. 14. As in Fig. 13, but for the 28–29 Nov 2001 case. The period between the vertical lines corresponds to the time intervals shown in Figs. 9 and 12.

by vertically pointing radar were a manifestation of turbulence associated with the wind shear in the frontal system passing over the Cascades.

When the Richardson number [$\mathrm{Ri} = N_m^2(du/dz)^{-2}$, where N_m is the moist Brunt–Väisälä frequency] is less than 0.25, shear-induced turbulence can develop (Houze 1997). For the 13–14 December case, Fig. 7c indicates Ri was below 0.25 in the layer between 2 and 2.5 km, consistent with the occurrence of shear-induced turbulence. There are also some other locations where Ri went below 0.25, however they were very thin layers. In the 28–29 November case Ri goes below critical between 2 and 2.8 km and between 0.75 and 1.25 km (Fig. 7f). Figures 13c and 14c indicate the maximum magnitudes of the radial velocity updrafts in the 2–3-km layer as a function of time in the regions where the reflectivity exceeded a threshold value of -2 dBZ. Since the maximum values regularly reached magnitudes of several meters per second, with 2 m s^{-1} being typical, the updraft velocities were sufficient to produce large supercooled cloud liquid water contents and hence riming. Rimed particles, even graupel, would be consistent with these drafts. The highly variable vertical velocities also would favor aggregation. Through the turbulent cascade of energy, variability in the vertical velocities field in the 1–3-km scale would be passed down to smaller scales, and particles would be driven into each other by the highly variable smaller-scale air motions. Moreover, these turbulent air motions were in a layer where the temperature would also favor aggregation (Hobbs 1974; Houze 1993).

Figures 13d and 14d show the time–height variability of the frequency of occurrence of dry aggregates or graupel according to the S-Pol polarimetric particle identification algorithm. These signals registered when the shear was strongest (Figs. 13a and 14a), the frequency of occurrence of radial velocity updrafts was greatest (Figs. 13b and 14b), and the intensity of the drafts was highest (Figs. 13c and 14c). The lag time between the occurrence of dry aggregates or graupel and the stronger updrafts can be reconciled by considering that the S-Pol radar, which measured particle types, was located upstream of the vertically pointing radar, which measured the updrafts. This coincidence of key dynamical and microphysical variables observed by three different instruments (the wind profiler, the vertically pointing radar, and the polarimetric scanning S-Pol radar) strongly suggests that the highly turbulent air motions above (and probably also below) the melting layer were promoting both aggregation and riming of ice particles. The turbulence in this layer could thus account for the maxima of dry aggregates and/or graupel in this layer. The persistence of this layer of turbulence provided an environment in which ice particles could aggregate to form larger particles that would be larger targets for riming by collection of supercooled cloud liquid water drops. The turbulence also created pockets of high liquid water contents within which the large aggregates could grow by riming and thus increase their fall speeds. Turbulence could thus have been a crucial component of the windward-side orographic enhancement of the precipitation in these storms by providing mechanisms by which particles would both be more likely to aggregate and more able to grow by riming, thus facilitating the fallout of precipitation particles on the lower windward slopes before being advected up to and over the crest of the mountain range.

f. Ice particles, liquid water content, and vertical air motions along the aircraft flight track

The evidence presented so far in this paper suggests that in the 2–3-km-altitude layer, just above the 0°C level, growth of graupel and/or dry aggregates is facilitated by the occurrence of mechanically induced turbulent updraft motions in the upslope flow as the frontal system advances over the windward slopes of the Cascades. In this section, we present aircraft data collected in this layer.

Figure 15 shows the only flight-track segment in which ice particles were collected in the layer of interest in either of the two cases described herein. This track was flown by the NOAA WP-3D aircraft, and it is overlaid on radar data in Fig. 15 showing that the aircraft was in the main precipitation layer during this time. The aircraft was flying between 2 and 2.8 km (mostly at 2 km) on this flight segment. Figure 16a shows the altitude as a function of time along with other key variables during part of the flight shown in Fig. 15. In this subsegment, the altitude decreased from slightly above 2.5–2 km (green line). The air temperature (blue line) increased from about -3.0°C to about 1°C during the time shown, that is, the aircraft crossed the 0°C level and encountered precipitation particles falling from just above that level, where the turbulent motions were indicated by the vertically pointing radar (Figs. 11b and 13). The vertical velocity trace (red line) indicates that the aircraft entered a region of increased turbulence around 0125 UTC 14 December 2001, that is, when it descended to an altitude close to 2.1 km. Magnitudes of vertical air velocities of 1 m s^{-1} were common and occasionally reached 4 m s^{-1} during the time interval between 0125–0130 UTC 14 December 2001. For this time period, cloud liquid water contents measured by the Johnson–Williams probe ranged from 0.1 to 0.6 g m^{-3}. After 0130 UTC 14 December 2001, the turbulence signal in the vertical velocity measurements decreased and

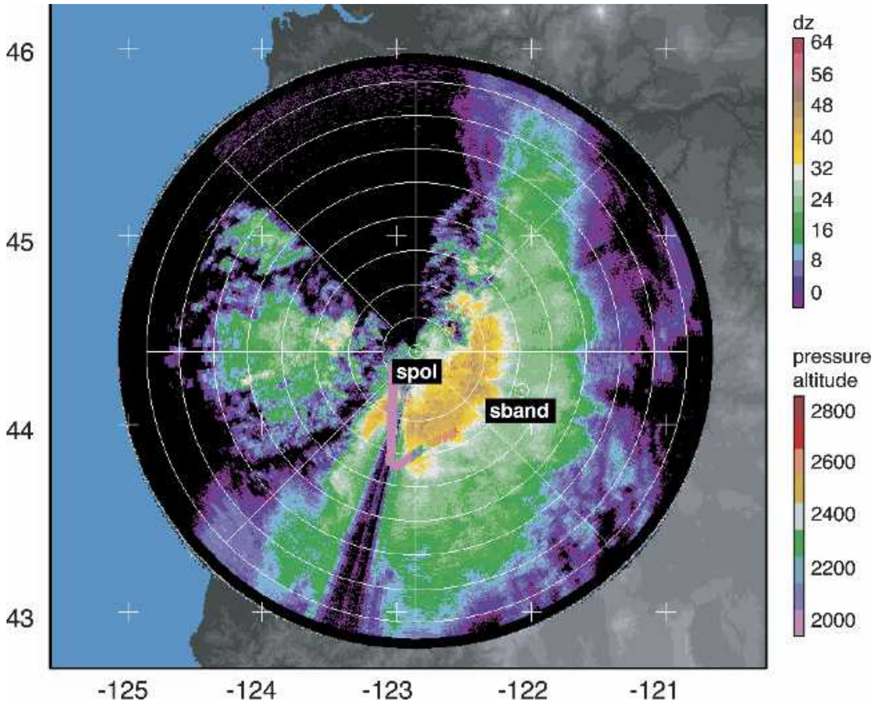

FIG. 15. The 1.5° PPI of S-Pol reflectivity at 0106 UTC 14 Dec 2001. The WP-3D flight track from 0120–0135 UTC 14 Dec 2001 is shown with color-coded altitude (m). The range ring spacing is 20 km.

so did the liquid water contents. Figure 16b shows the same data as Fig. 16a but with a five-point running mean filter applied to the time series (except for altitude). In this trace, there is an association between cloud liquid water content and vertical velocity. Whenever the cloud liquid water content exceeded 0.4 g m^{-3}, the vertical velocity was over 1 m s^{-1}, suggesting that the turbulent updrafts were producing pockets of moderate cloud liquid water content that would have been available for riming. Since these cloud liquid water contents were not particularly high, we would expect moderate rather than heavy riming of ice particles. In Fig. 16c, a 2-min segment of Fig. 16b was expanded. In addition to the correlation between cloud liquid water and vertical velocity, an anticorrelation of these variables with the air temperature was observed. This behavior indicates that the turbulence was mechanical rather than buoyant in nature. The typical flight-track duration of the updrafts was ~8 s, which for an airspeed of ~100 m s^{-1} corresponds spatially to ~0.8 km, which is consistent with the cell size derived from vertically pointing radar data (Fig. 11b).

The S-Pol radar indicated that reflectivity values associated with the polarimetrically inferred graupel and/or dry aggregates were as large as 45 dB*Z*. To determine if this rather high reflectivity was consistent with the inferred particle types, we examined the Particle Measuring System probe data collected by the NOAA WP-3D from 0126 to 0127 UTC 14 December 2001, a period when the aircraft was flying at an elevation of 2 km and in subzero temperatures (Fig. 16). Figure 17a shows the 2D-P probe particle number density spectrum. The accumulated reflectivity associated with this distribution was calculated following Vivekanandan et al. (1994; Fig. 17b). The density values used to calculate the reflectivity correspond to observed values (Locatelli and Hobbs 1974). The series of curves in Fig. 17b indicate the dependence of the reflectivity produced by the distribution on the density of the ice particles. The total reflectivity produced by the distribution fluctuates between 25 and 55 dB*Z*, depending on the degree of riming. This calculation indicates that if the observed particles had densities between those of graupel-like snow of lump type and conical graupel they would have produced reflectivity values of ~45 dB*Z*, corresponding to the radar-observed reflectivity at this level. Ice particle images seen on the PMS probes (Fig. 18) frequently appeared to be aggregates, as inferred from the predominant characteristic of irregular shapes with open gaps. Since the open gaps were often filled in and somewhat blobby in appearance, we further infer that the aggregates were often rimed. Occasionally, the im-

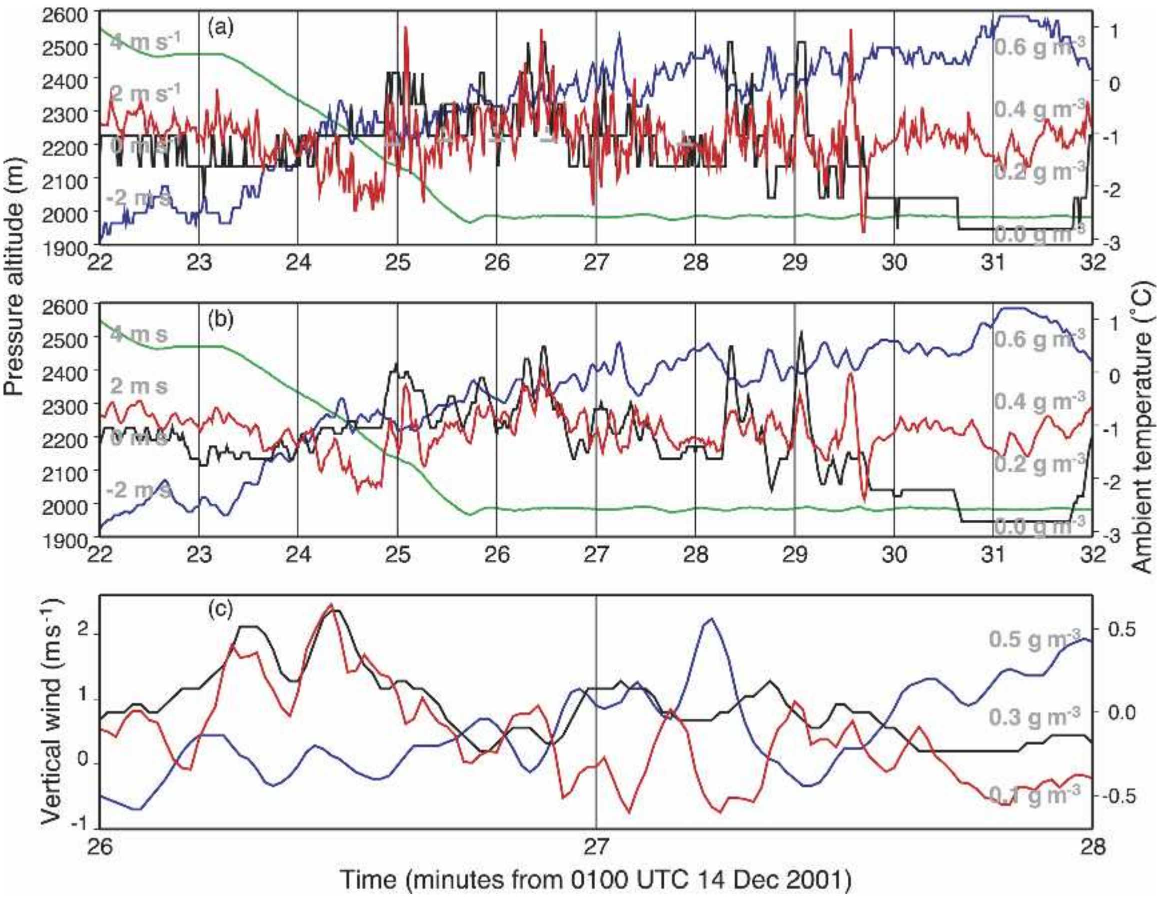

FIG. 16. (a) WP-3D flight-track data collected during a segment of the flight shown in Fig. 15. Pressure altitude (green line), air temperature (blue line), vertical wind (red line), and cloud liquid water (black line) are shown. (b) As in (a) but with a five-point running mean filter applied to all variables except pressure altitude. (c) As in (b) zooming in over a 2-min segment.

ages were completely filled in with smoother edges and could be inferred to be graupel. Thus, the ice particle images collected on board the aircraft were consistent with the presence of rimed aggregates and/or graupel falling out of the layer of turbulent air motions seen in the vertically pointing radar data. These ice particle samples furthermore appear to be consistent with the particle types indicated by the S-Pol polarimetric variables and also with the heavily rimed aggregates of graupel-like snow collected at Ray Benson Sno-Park, a ground-based observational site located at an elevation of 1454 m (Woods et al. 2005).

4. Comparison with the MAP IOP8 case

The similarity of the IMPROVE-2 cases (as brought out by Figs. 13 and 14) indicates that the processes seen in these storms are repeatable. To address further the repeatability of these results, we refer to IOP8 of MAP, which was a case in which the low-level flow was profoundly blocked (Rotunno and Ferretti 2003; Bousquet and Smull 2003; Medina and Houze 2003). The synoptic situation is summarized in Fig. 19. A 500-hPa trough was moving over the Alps from the west. The 840-hPa flow ahead of the upper trough was impinging on the Alps just above the layer of stable blocked flow. The S-Pol reflectivity, radial velocity, and particle microphysics cross section taken roughly parallel to the 840-hPa flow and normal to the mountain range (line shown in Fig. 1b) is shown in Fig. 20. The cross-barrier flow was similar to that observed in the IMPROVE-2 cases in the sense that a layer of highly sheared flow was present at low levels (cf. Figs. 8 and 9). However, the upstream conditions below the shear layer in IOP8 differed from those in IMPROVE-2. During IOP8 the cross-barrier flow component at low levels (up to 1 km) was sometimes directed away from the mountains, denoting strongly blocked flow (Bousquet and Smull 2003; Steiner et al. 2003). For the IMPROVE-2 cases, the cross-barrier flow component at low levels ap-

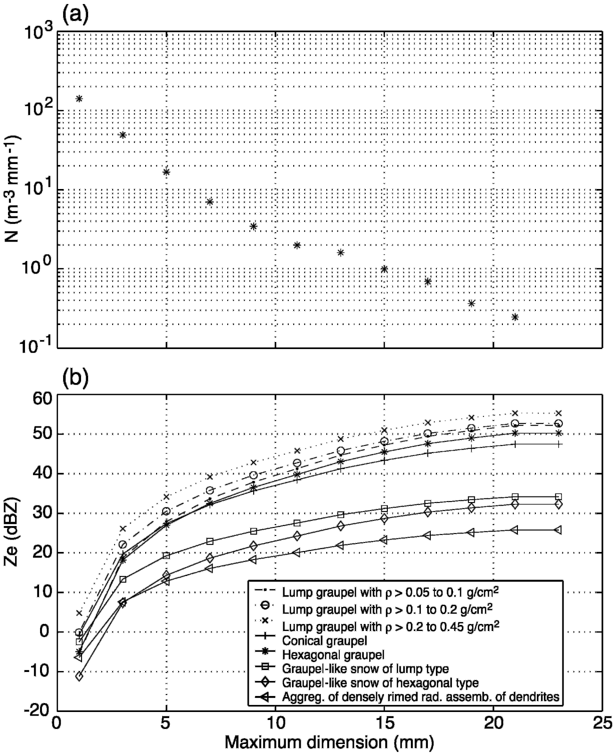

FIG. 17. (a) Particle number density spectrum from WP-3D 2DP PMS probe from 0126 to 0127 UTC 14 Dec 2001. (b) Accumulated reflectivity produced by the spectrum in (a) for different densities of rimed particles. The densities used are from Locatelli and Hobbs (1974).

peared to be slowed down or partially blocked by the terrain, but the low-level cross-barrier flow component was generally directed toward the crest.

The polarimetrically derived hydrometeor types in Fig. 20c exhibited graupel and/or dry aggregates and the vertically pointing data of the Swiss ETH radar located at Macugnaga (Fig. 1b; VP) showed finescale variation of the reflectivity (fallstreaks) and rapidly repeating updraft cells in the 2–4-km layer (Fig. 21). The cellularity in the vertically pointing radar data in Fig. 21 is similar to that seen in the IMPROVE-2 cases (Figs. 11 and 12). During IOP8, the atmosphere was strongly stable in the altitude range in which the cells occurred (Fig. 8 of Medina and Houze 2003), ruling out the possibility of buoyant instability playing a role in producing the updraft cells. The VP radar was located inside a valley and at 70 km from the S-Pol radar. Therefore, because of beam blocking effects and the decrease of resolution due to beam widening with range, it was not possible for the S-Pol radar to resolve the shear layer directly over the Macugnaga site. However, data from the WP-3D aircraft (Medina et al. 2005) indicate the presence of a shear layer at altitudes of 2–3 km at 70-km ranges from the S-Pol location, which corresponds to the altitude range in which the cells occurred. These observations indicate the occurrence of cellular overturning in a stable, sheared layer over the windward slope of the Alps, as was the case in the IMPROVE-2 storms. This type of pattern, which can enhance the growth of ice particles over the windward slopes, thus appears to be a highly repeatable phenomenon in certain baroclinic storms passing over mountain ranges.

5. Summary

A highly simplified picture of the mechanism of orographic enhancement of widespread frontal precipitation elucidated by this study is summarized in Fig. 22. The figure represents a vertical cross section perpendicular to a barrier, extending from the lowlands to the crest, when a widespread, deep, stable precipitating cloud of a frontal system is passing over the windward slope of the mountain range. In some cases, as the large-scale precipitating system reaches the upward slopes, the low-level cross-barrier flow component (below ~1 km) decelerates, while the along-barrier component apparently accelerates; that is, the low-level flow is partially blocked. The IMPROVE-2 and MAP IOP8 cases described in this paper are examples of this type of storm. In storms with less stable low-level flow, air may ascend readily over the terrain with no shear layer bounding a lower-level weak or blocked flow (Medina and Houze 2003).

The flow layer above the lower, stable, retarded, or blocked flow is stronger and able to cross the mountain barrier. A sheared layer is thus formed above the low-level flow. The layer of shear is observed to slope upward, following the general slope of the terrain. The combination of high shear and stability in this layer produces conditions that support turbulent cells ($Ri < 0.25$). Transient oscillations triggered by the flow of stable air over the rough lower boundary may also contribute to the formation of the turbulent cells; however, such a process is not yet well described theoretically. The updraft cells located in the stable sheared layer atop the retarded or blocked flow operate within the deep, broad precipitating cloud of the large-scale baroclinic system. The widespread deep cloud is producing snow in response to the dynamics of the baroclinic frontal disturbance that is moving over the mountain range. As the frontal system traverses the mountain range, additional lifting owing to the ascent over the mountain range produces condensate over and above that produced by the baroclinic system dynamics alone. The layer of cells that form in the sheared layer are embedded in the larger cloud system, and they act to concentrate the additional condensate produced by orographic

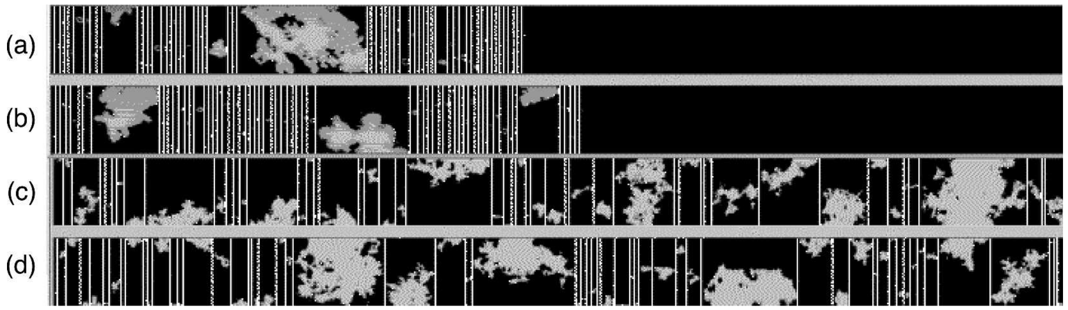

FIG. 18. Ice particle imagery taken with PMS probes on a NOAA WP-3D aircraft at an altitude of 2 km (~60 km to the south of the S-Pol radar) at 0126 UTC 14 Dec 2001 with (a), (b) 2DC probe (width = 1.6 mm) and (c), (d) 2DP probe (width = 9.6 mm).

lifting into pockets of high liquid water content associated with the small-scale updraft cells. Aggregation of the ice particles falling from the broader deep frontal cloud into the layer of cells is aided by the turbulent air motions associated with the cells. The aggregate snow-

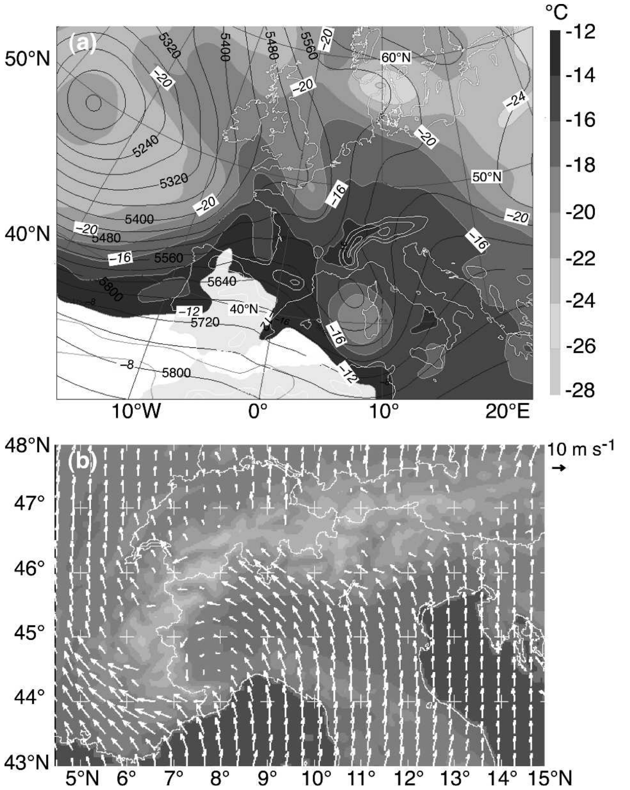

FIG. 19. (a) European Centre for Medium-Range Weather Forecasts 500-hPa geopotential height (black lines) and air temperature (shading) forecasts over Europe for 1200 UTC 21 Oct 1999. White contours within the landmasses show land mask and the topography of mountain ranges. (b) The atmospheric Mesoscale Compressible Community numerical forecast model (MC2) topography and storm-mean 840-hPa wind field around the Alps during IOP8 (1200–2200 UTC 20 Oct 1999). Gray shades indicate the topography. (From Medina and Houze 2003.)

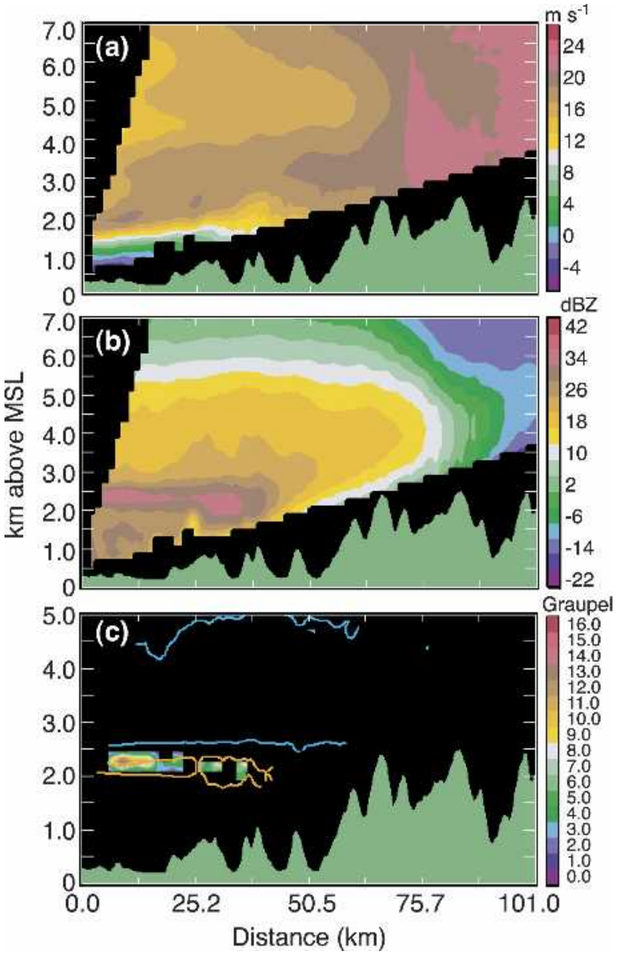

FIG. 20. Vertical cross section of NCAR S-Pol radar data extending from the radar site, located on the lower-left corner of the panels, across the Alps to the northwest. The topography is shown in the lower part of each panel. The fields in the panels have been either averaged or accumulated over a 3-h period, from 0800 to 1100 UTC 21 Oct 1999. (a) Mean radial velocity, with positive (negative) values denoting flow away from (toward) the radar, (b) mean reflectivity, (c) frequency of occurrence of particle types: 75% of snow (cyan), 60% of melting aggregates (orange), and graupel or dry aggregates (shading).

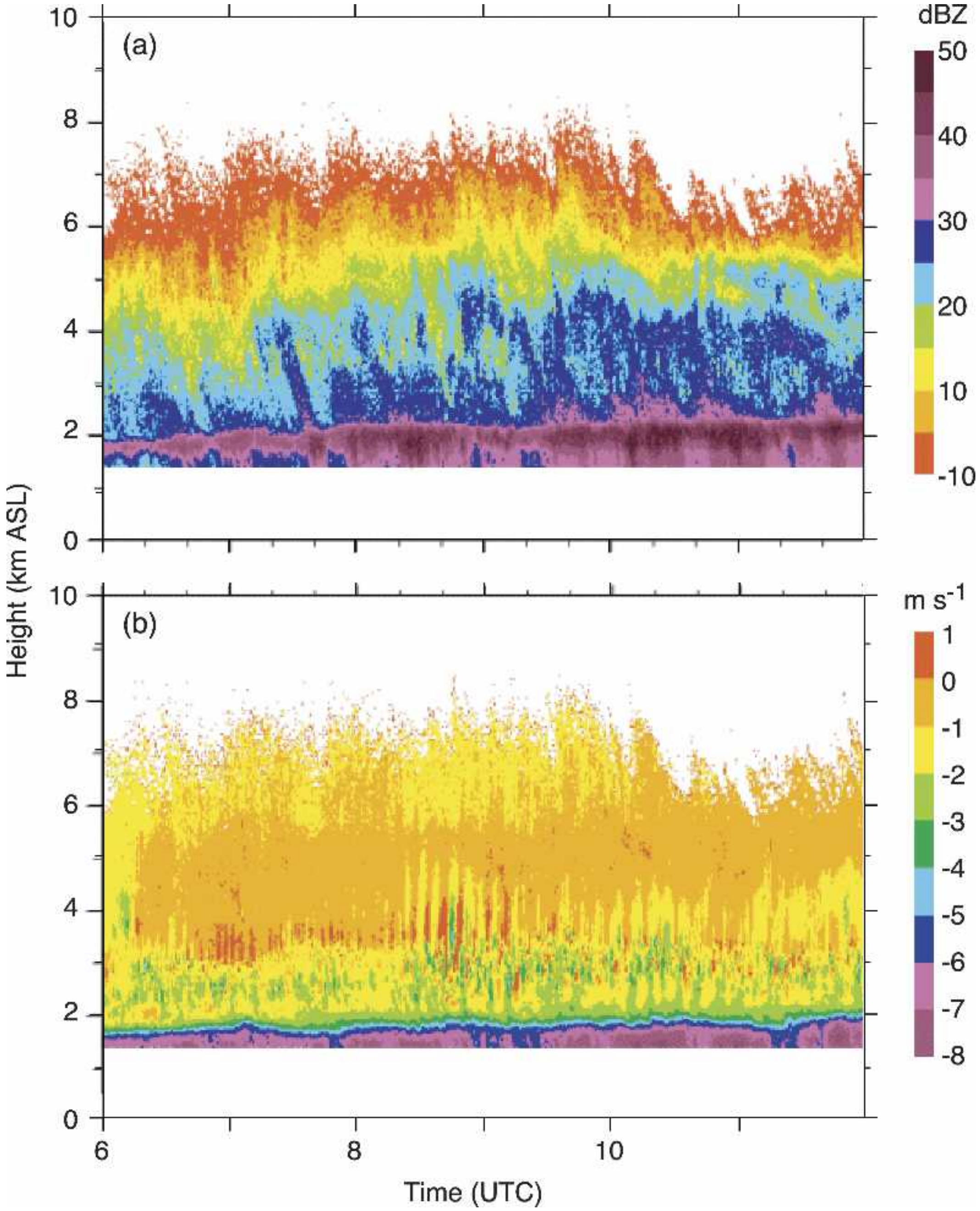

FIG. 21. Data from the ETH X-band VP radar, located at Macugnaga during MAP. The data shown are for 0600–1200 UTC 21 Oct 1999. (a) Reflectivity and (b) radial velocity with positive (negative) values denoting flow away from (toward) the radar. The red pixels show regions where the radial velocity >0 m s^{-1} upward. (Figure courtesy of the MAP Data Center.)

flakes are large targets for riming by collection and accretion of supercooled cloud drops when the aggregates find themselves within the cellular pockets of high cloud liquid water content. The aggregates and other ice particles thus acquire greater mass and fall out quickly. In this way the additional condensate produced by orographic lifting can quickly reach the ground on the lower windward slopes. Without the aid of the cells, the condensate would not likely fall out until it was carried downstream, higher up on the ridge or even on the lee side (as demonstrated by Hobbs et al. 1973).

Since the sloped shear layer may cross the 0°C level,

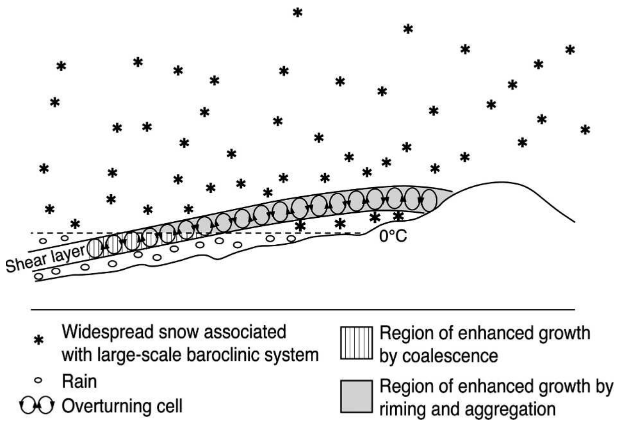

FIG. 22. Conceptual model of the dynamical and microphysical mechanisms responsible for the orographic enhancement of precipitation during storms with stable stratification.

the microphysical processes of growth enhancement vary. Below the 0°C level, the accretion may take the form of coalescence, as the melted snow from above falls through the cells of enhanced liquid water content. Above the 0°C level, the snow particles from above grow by riming as they pass downward through the cells. In addition, the layer of turbulence increases the likelihood of collision and aggregation of the ice particles. Larger aggregates, when rimed, produce heavier, faster-falling hydrometeors. Rimed aggregates and graupel (both observed by aircraft, section 3f) are the ice particle types most likely in this growth environment. Riming, aggregation, and coalescence engendered by the turbulence in the shear layer all contribute to the production of heavy particles that fall out more quickly over the windward slopes than they would in the absence of the cells.

6. Conclusions

When the precipitation-producing airflow of a baroclinic storm impinges on a mountain range, the condensate produced by the orographic lifting superimposed on the baroclinic cloud system must fall out quickly to explain the enhanced precipitation amounts that are observed on the lower windward slopes. The microphysical processes of precipitation growth must act quickly to wring the orographically engendered condensate out of the air before the hydrometeors produced by the orographic uplift are carried up and over the mountain range. Small-scale cellular overturning motions can catalyze the enhanced microphysical growth by providing pockets of higher liquid water content in the cells within the broader frontal cloud. The liquid water in the cells can be collected by the precipitation particles falling from the frontal cloud, causing them to become heavier and to fall out more quickly.

Cellular motions can form within a layer of the precipitating frontal cloud if the orographically lifted airflow in that layer is conditionally unstable (Medina and Houze 2003). The present study shows that even if the flow impinging on the mountain range, as part of a baroclinic system passing over the range, is stable, it can nevertheless organize itself to produce a layer of small-scale cellular overturning. At low levels the stable flow is likely to be retarded or blocked. Thus, the cross-barrier component of the flow at low levels is greatly reduced. This layer of weak (or negative) cross-barrier flow is bounded above by a layer of strong shear, separating the retarded or partially blocked low-level cross-barrier flow from the unblocked cross-barrier flow at higher levels. In the shear layer, finescale repeating updraft cells occur and are seen especially well by vertically pointing Doppler radar. These cells are either shear-induced turbulence or buoyancy oscillations in the shear layer that are forced by the rough lower terrain. In either case, buoyant instability is not required.

Thus, nearly any baroclinic system passing over a mountain range has the capacity to produce cellular overturning over the windward slope of the range regardless of its stability characteristics. The cells, in turn, invigorate the microphysical processes by facilitating growth by coalescence, riming, and aggregation of precipitation particles falling from the higher levels of the frontal cloud. In this way the condensate provided to the frontal cloud system by orographic lifting is quickly removed from the cloud in the form of windward-slope precipitation. We suggest that this mechanism may be one of the reasons that mountain ranges exposed to baroclinic storms tend to have climatological precipitation maxima on the windward slopes.

Acknowledgments. The authors would like to acknowledge Bradley Smull, J. Vivekanandan, Scott Ellis, Sandra Yuter, Clifford Mass, and three anonymous reviewers for their helpful comments and suggestions. Tom Wilson provided software to peruse and output the aircraft particle image data. Candace Gudmundson edited the manuscript and Kay Dewar and Beth Tully enhanced the figures. Stacy Brodzik provided data managing and engineering support. Matt Garvert provided MM5 upstream soundings. Sean Casey and Janae Nash assisted in the processing of radar data. This research was sponsored by the National Science Foundation under Grant ATM-0221843.

REFERENCES

Austin, P. M., and A. C. Bemis, 1950: A quantitative study of the "bright band" in radar precipitation echoes. *J. Meteor.,* **7,** 145–151.

Bader, M. J., S. A. Clough, and G. P. Cox, 1987: Aircraft and dual polarization radar observations of hydrometeors in light stratiform precipitation. *Quart. J. Roy. Meteor. Soc.,* **113,** 491–515.

Bargen, D. W., and R. C. Brown, 1980: Interactive radar velocity unfolding. Preprints, *19th Conf. on Radar Meteorology*, Miami Beach, FL, Amer. Meteor. Soc., 278–283.

Battan, L. J., 1973: *Radar Observations of the Atmosphere*. University of Chicago Press, 279 pp.

Bougeault, P., and Coauthors, 2001: The MAP Special Observing Period. *Bull. Amer. Meteor. Soc.,* **82,** 433–462.

Bousquet, O., and B. F. Smull, 2003: Observations and impacts of upstream blocking during a widespread orographic precipitation event. *Quart. J. Roy. Meteor. Soc.,* **129,** 391–409.

Drummond, F. J., R. R. Rogers, S. A. Cohn, W. L. Ecklund, D. A. Carter, and J. S. Wilson, 1996: A new look at the melting layer. *J. Atmos. Sci.,* **53,** 759–769.

Durran, D. R., and J. B. Klemp, 1982: On the effects of moisture on the Brunt–Väisälä frequency. *J. Atmos. Sci.,* **39,** 2152–2158.

Fabry, F., and I. Zawadzki, 1995: Long-term observations of the melting layer of precipitation and their interpretation. *J. Atmos. Sci.,* **52,** 838–851.

Frei, C., and C. Schaer, 1998: A precipitation climatology of the Alps from high-resolution raingauge observations. *Int. J. Climatol.,* **18,** 873–900.

Garvert, M. F., B. A. Colle, and C. F. Mass, 2005: The 13–14 December 2001 IMPROVE-2 event. Part I: Synoptic and mesoscale evolution and comparison with a mesoscale model simulation. *J. Atmos. Sci.,* **62,** 3474–3492.

Hann, J., 1902: Increase of rainfall with altitude. *Mon. Wea. Rev.,* **30,** 218–220.

Henry, A. J., 1902: Average annual precipitation in the United States for the period 1871 to 1901. *Mon. Wea. Rev.,* **30,** 207–213, 241.

——, 1919: Increase of precipitation with altitude. *Mon. Wea. Rev.,* **47,** 33–41.

Hill, S. A., 1881: The meteorology of the North-West Himalaya. *Memoirs,* Vol. 1, India Meteor. Dept., 377–426.

Hobbs, P. V., 1974: *Ice Physics.* Oxford University Press, 837 pp.

——, 1975: The nature of winter clouds and precipitation in the Cascade Mountains and their modification by artificial seeding. Part I: Natural conditions. *J. Appl. Meteor.,* **14,** 783–804.

——, R. C. Easter, and A. B. Fraser, 1973: A theoretical study of the flow of air and fallout of solid precipitation over mountainous terrain. Part II: Microphysics. *J. Atmos. Sci.,* **30,** 813–823.

——, R. A. Houze Jr., T. Matejka, L. F. Radke, D. G. Atkinson, and R. R. Weiss, 1974: The dynamical and microphysical structure of an occluded frontal system and its modification by orography. University of Washington, Research Rep. IX, 127 pp.

Houze, R. A., Jr., 1993: *Cloud Dynamics*. Academic Press, 573 pp.

——, 1997: Stratiform precipitation in regions of convection: A meteorological paradox? *Bull. Amer. Meteor. Soc.,* **78,** 2179–2196.

Locatelli, J. D., and P. V. Hobbs, 1974: Fall speeds and masses of solid precipitation particles. *J. Geophys. Res.,* **79,** 2185–2197.

Marwitz, J. D., 1987: Deep orographic storms over the Sierra Nevada. Part II: The precipitation processes. *J. Atmos. Sci.,* **44,** 174–185.

Medina, S., and R. A. Houze Jr., 2003: Air motions and precipitation growth in alpine storms. *Quart. J. Roy. Meteor. Soc.,* **129,** 345–371.

——, B. Smull, R. A. Houze Jr., and M. Steiner, 2005: Cross-barrier flow during orographic precipitation events: Results from MAP and IMPROVE. *J. Atmos. Sci.,* **62,** 3580–3598.

Oye, R., C. Muller, and S. Smith, 1995: Software for radar translation, visualization, editing, and interpolation. Preprints, *27th Conf. on Radar Meteorology*, Vail, CO, Amer. Meteor. Soc., 359–361.

Peck, E. L., and M. J. Brown, 1962: An approach to the development of isohyetal maps for mountainous areas. *J. Geophys. Res.,* **67,** 681–694.

Reed, W. G., and J. B. Kincer, 1917: The preparation of precipitation charts. *Mon. Wea. Rev.,* **45,** 233–235.

Rotunno, R., and R. Ferretti, 2003: Orographic effects on rainfall in MAP cases IOP 2B and IOP 8. *Quart. J. Roy. Meteor. Soc.,* **129,** 373–390.

Smith, R. B., 1979: The influence of mountains on the atmosphere. *Advances in Geophysics,* Vol. 21, Academic Press, 87–230.

Steiner, M., O. Bousquet, R. A. Houze, B. F. Smull, and M. Mancini, 2003: Airflow within major alpine river valleys under heavy rainfall. *Quart. J. Roy. Meteor. Soc.,* **129,** 411–432.

Stoelinga, M. T., and Coauthors, 2003: Improvement of Microphysical Parameterization through Observational Verification Experiment. *Bull. Amer. Meteor. Soc.,* **84,** 1807–1826.

Straka, J. M., D. S. Zrnic, and A. V. Ryzhkov, 2000: Bulk hydrometeor classification and quantification using polarimetric radar data: Synthesis of relations. *J. Appl. Meteor.,* **39,** 1341–1372.

Vivekanandan, J., V. N. Bringi, M. Hagen, and P. Meischner, 1994: Polarimetric radar studies of atmospheric ice particles. *IIEE Trans. Geosci. Remote Sens.,* **32,** 1–10.

——, D. S. Zrnic, S. M. Ellis, R. Oye, A. V. Ryzhkov, and J. Straka, 1999: Cloud microphysics retrieval using S-band dual-polarization radar measurements. *Bull. Amer. Meteor. Soc.,* **80,** 381–388.

Wakimoto, R. M., and V. N. Bringi, 1988: Dual-polarization observations of microbursts associated with intense convection: The 20 July storm during the MIST Project. *Mon. Wea. Rev.,* **116,** 1521–1539.

Weiss, R. R., and P. V. Hobbs, 1975: The use of a vertically pointing pulsed Doppler radar in cloud physics and weather modification studies. *J. Appl. Meteor.,* **14,** 222–231.

White, A. B., J. R. Jordan, B. E. Martner, F. M. Ralph, and B. W. Bartram, 2000: Extending the dynamic range of an S-band radar for cloud and precipitation studies. *J. Atmos. Oceanic Technol.,* **17,** 1226–1234.

Willis, P. T., and A. J. Heymsfield, 1989: Structure of the melting layer in mesoscale convective system stratiform precipitation. *J. Atmos. Sci.,* **46,** 2008–2025.

Woods, C. P., M. T. Stoelinga, J. D. Locatelli, and P. V. Hobbs, 2005: Microphysical processes and synergistic interaction between frontal and orographic forcing of precipitation during the 13 December 2001 IMPROVE-2 event over the Oregon Cascades. *J. Atmos. Sci.,* **62,** 3493–3519.

Zeng, Z., S. E. Yuter, R. A. Houze Jr., and D. E. Kingsmill, 2001: Microphysics of the rapid development of heavy convective precipitation. *Mon. Wea. Rev.,* **129,** 1882–1904.